

Highlights of Joint Research

Supercomputer Center

The Supercomputer Center (SCC) is a part of the Materials Design and Characterization Laboratory (MDCL) of ISSP. Its mission is to serve the whole community of computational condensed-matter physics of Japan providing it with high performance computing environment. In particular, the SCC selectively promotes and supports large-scale computations. For this purpose, the SCC invites proposals for supercomputer-aided research projects and hosts the Steering Committee, as mentioned below, that evaluates the proposals.

The ISSP supercomputer system consists of three subsystems: System A, which is intended for a parallel computation with relatively smaller number of nodes connected tightly, and System B, which is intended for more nodes with relatively loose connections. In July, 2010, the SCC replaced the two supercomputer subsystems. The current system B is SGI Altix ICE 8400EX, which consists of 30 racks or 15360 cores whereas the system A is NEC SX-9, which consists of 4 nodes or 64 cpus. They have totally 200 TFlops. System C - FUJITSU PRIMEHPC FX10 was installed in April, 2013. It is highly compatible with K computer, the largest supercomputer in Japan. System C consists of 384 nodes, and each node has 1 SPARC64TM IXfx CPU (16 cores) and 32 GB of memory. The total system achieves 90.8 TFlops theoretical peak performance.

The hardware administration is not the only function of the SCC. The ISSP started hosting Computational Materials Science Initiative (CMSI), a new activity of promoting materials science study with next-generation parallel supercomputing. This activity is financially supported by the MEXT HPCI strategic program, and in CMSI, a number of major Japanese research institutes in various branches of materials science are involved. The SCC supports the activities of CMSI as its major mission.

All staff members of university faculties or public research institutes in Japan are invited to propose research projects (called User Program). The proposals are evaluated by the Steering Committee of SCC. Pre-reviewing is done by the Supercomputer Project Advisory Committee. In school year 2013 totally 245 projects were approved. The total points applied and approved are listed on Table. 1 below.

The research projects are roughly classified into the following three (the number of projects approved):

- First-Principles Calculation of Materials Properties (107)
- Strongly Correlated Quantum Systems (30)
- Cooperative Phenomena in Complex, Macroscopic Systems (86)

All the three involve both methodology of computation and its applications. The results of the projects are reported in 'Activity Report 2013' of the SCC. Every year 3-4 projects are selected for "invited papers" and published at the beginning of the Activity Report. In the Activity Report 2013, the following three invited papers are included:

- "One-hundred-million-atom electronic structure calculations on the K computer", Takeo HOSHI
- "Strong correlation of electrons studied by computational approaches—Physics of superconductors and topological phases", Shiro SAKAI, Takahiro MISAWA, Youhei YAMAJI, Mayuru KURITA, and Masatoshi IMADA
- "Coarse-Grained Simulation of Surfactant Membrane", Hayato SHIBA and Hiroshi NOGUCHI

Class	Max/Min Points	Application	Number of Projects	Total Points					
				Applied			Approved		
				System A	System B	System C	System A	System B	System C
A	100	any time	10	350	850	500	350	850	500
B	2k, 1k, 500	twice a year	56	40.7k	45.0k	6.6k	28.7k	29.8k	5.8k
C	20k, 10k, 2.5k	twice a year	130	793.5k	1043.0k	146.9k	486.5k	391.0k	98.6k
D	20k, 10k, 2.5k	any time	3	0	22.0k	0	0	19.0k	0
E	0, 30k, 2.5k	twice a year	24	-	653.0k	43.8k	-	283.5k	36.6k
S		twice a year	0	0	0	0	0	0	0
CMSI			22	-	-	-	-	-	92.5k
Total			245	834.6k	1,763.9k	197.8k	515.6k	724.2k	144.0k

Table 1. Research projects approved in 2013

The maximum points allotted to the project of each class are the sum of the points for the two systems; Computation for 1 CPU•hour corresponds to 0.32, 0.022, and 0.042 points for System-A, System-B, and System C, respectively.

Neutron Science Laboratory

The Neutron Science Laboratory (NSL) has been playing a central role in neutron scattering activities in Japan since 1961 by performing its own research programs as well as providing a strong General User Program for the university-owned various neutron scattering spectrometers installed at the JRR-3 (20MW) operated by Japan Atomic Energy Agency (JAEA) in Tokai (Fig. 1). In 2003, the Neutron Scattering Laboratory was reorganized as the Neutron Science Laboratory to further promote the neutron science with use of the instruments in JRR-3. Under the General User Program supported by NSL, 14 university-group-owned spectrometers in the JRR-3 reactor are available for a wide scope of researches on material science, and proposals close to 300 are submitted each year, and the number of visiting users under this program reaches over 6000 person-day/year. In 2009, NSL and Neutron Science Laboratory (KENS), High Energy Accelerator Research Organization (KEK) built a chopper spectrometer, High Resolution Chopper Spectrometer, HRC, at the beam line BL12 of MLF/J-PARC (Materials and Life Science Experimental Facility, J-PARC). HRC covers a wide energy and Q-range ($10\mu\text{eV} < \hbar\omega < 2\text{eV}$ and $0.02\text{\AA}^{-1} < Q < 50\text{\AA}^{-1}$), and therefore becomes complementary to the existing inelastic spectrometers at JRR-3. HRC started to accept general users through the J-PARC proposal system in FY2011.

Triple axis spectrometers, HRC, and a high resolution powder diffractometer are utilized for a conventional solid state physics and a variety of research fields on hard-condensed matter, while in the field of soft-condensed matter science, researches are mostly carried out by using the small angle neutron scattering (SANS-U) and/or neutron spin echo (iNSE) instruments. The upgraded time-of-flight (TOF) inelastic scattering spectrometer, AGNES, is also available through the ISSP-NSL user program.

On March 11, 2011, a great earthquake with Magnitude 9.0 hit North East Coast of Japan. Fortunately, JRR-3 was under regular inspection and no serious accidents or damages were reported. However, the lifeline of Tokai Village area was lost for more than two weeks, and it took more than two months before damage inspection of JRR-3 could be started. As of May of 2014, JRR-3 has not restarted yet. General User Programs of 2012 and 2013 were cancelled and that of 2014 has been suspended so far. In order to compensate the



Fig. 1. The reactor of JRR-3. The eight neutron scattering instruments are attached to the horizontal beam tubes in the reactor experimental hall. Two thermal and three cold guides are extracted from the reactor core towards the guide hall located to the left.



Fig. 2. The U.S.-Japan spectrometer, CTAX, installed at the cold guide-line CG4, High Flux Isotope Reactor (HFIR), in Oak Ridge National Laboratory. Members who contributed the relocation project of the U.S.-Japan spectrometer celebrate the completion of the project in October 2010.

loss of the activity of NSL, a number of proposals accepted in 2011 - 2013 were transferred to overseas owing to kind offer from the major facilities, namely, ORNL, ILL, ANSTO, and HANARO.

The NSL also operates the U.S.-Japan Cooperative Program on neutron scattering, providing further research opportunities to material scientists who utilize the neutron scattering technique for their research interests. In 2010, relocation of the U.S.-Japan triple-axis spectrometer, CTAX, was completed, and it is now open to users (Fig. 2). <http://neutrons.ornl.gov/instruments/HFIR/CG4/>

The activity report on Neutron Scattering Research in JFY2011 is given in NSL-ISSP Activity Report vol. 18 (2011), http://quasi.issp.u-tokyo.ac.jp/actrep/actrep-18-2011/index_pub_vol18.html.

International MegaGauss Science Laboratory

The objective of this laboratory (Fig. 1) is to study the physical properties of solid-state materials (such as semiconductors, magnetic materials, metals, insulators, superconducting materials) under ultra-high magnetic field conditions. Such a high magnetic field is also used for controlling the new material phase and functions. Our pulse magnets, at moment, can generate up to 87 Tesla (T) by non-destructive manner, and from 100 T up to 760 T (the world strongest as



Fig. 1. Building view of the International MegaGauss Science Laboratory (C-building) at ISSP.



Fig. 2. The building for the flywheel generator (left hand side) and a long pulse magnet station (right hand side). The flywheel giant DC generator is 350 ton in weight and 5 m high (bottom). The generator, capable of a 51 MW output power with the energy storage 210 MJ, is planned to energize the long pulse magnet generating 100 T without destruction.

an in-door record) by destructive methods. The laboratory is opened for scientists both from Japan and from overseas, especially from Asian countries, and many fruitful results are expected to come out not only from collaborative research but also from our in-house activities. One of our ultimate goals is to provide the scientific users as our joint research with magnets capable of a 100 T, milli-second long pulses in a non-destructive mode, and to offer versatile physical precision measurements. The available measuring techniques now involve magneto-optical measurements, cyclotron resonance, spin resonance, magnetization, and transport measurements. Recently, specific heat and calorimetric measurements are also possible to carry out with sufficiently high accuracy.

Our standard non-destructive-type pulse magnets are energized by single capacitor bank and can generate fields up to 75 T for ordinary use. Their simple sinusoidal waveforms are advantageous for precise and reliable measurements of various physical properties. Several on-demand magnets

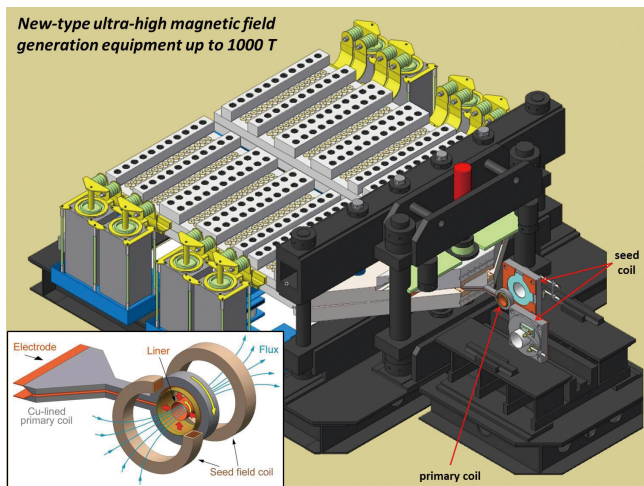


Fig. 3. (Build. C) The building for the electro-magnetic flux compression, generating over 700 T. 1000 T project started since 2010, and finally condenser banks of 9 MJ (5 MJ + 2 MJ + 2 MJ) as a main system with the 2 MJ sub bank system for the seed field have been installed, and completed in the year of 2014.

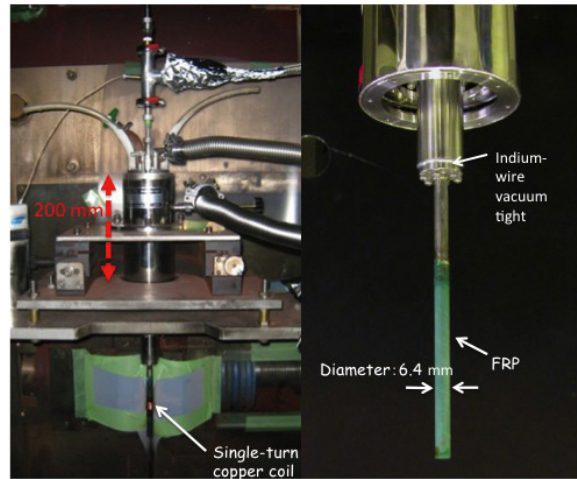


Fig. 4. A photo of the V-type single-turn coil equipped with 40 kV, (A:100+B:100=200 kJ) fast operating pulse power system. Measurements are carried out from room temperature down to 2 K by a specially designed cryostat.

having irregular shapes and sizes are developed for some particular experiments. We open six magnet cells for parallel experiments and accept more than 50 research projects per year in 2013.

A 210 MJ flywheel generator (Fig. 2), which is the world largest DC power supply (recorded in the Guinness Book of World Records) has been installed in the DC flywheel generator station at our laboratory, and used as an energy source of long pulse magnets. The magnet technologies are intensively devoted to the quasi-steady long pulse magnet (an order of 1-10 sec) energized by the giant DC power supply. The latest long-pulse magnet can generate fields up to 36 T with its pulse half-period of 1 sec.

Our interests cover the study on quantum phase transitions (QPTs) induced by high magnetic fields. Field-induced QPTs have been explored in various materials such as quantum spin systems, strongly correlated electron systems and other magnetic materials. Direct thermodynamic evidences of QPTs are obtained through magnetization and recently developed caloric measurements. For some QPTs, changes in symmetry at the transitions are sensitively resolved through measurements of electric polarization or optical imaging using a polarizing microscope. High resolution of electrical measurements realized the observation of quantum oscillations in high quality crystals through measurements of electrical resistivity, contactless impedance, and torque magnetometry.

Magnetic fields higher than 100 T can only be obtained with destructing a magnet coil, where ultra-high magnetic fields are obtained in a microsecond time scale. Our destructive techniques have undergone intensive developments. The project, financed by the ministry of education, culture, sports, science and technology, is now in progress, and goal is to generate 1000 T by the electromagnetic flux compression (EMFC) system (Fig. 3). The system which is unique to ISSP in the world scale is comprised of a power source of 5 MJ main condenser bank and 2 MJ condenser bank and has been accomplished its installation. Two magnet stations are constructed and both are energized from each power source. Both systems are fed with a 2 MJ condenser bank used for a seed-field coil, of which magnetic flux is to be compressed.

As an easy access to the megagauss science and technology, we have the single-turn coil (STC) system capable of generating the fields of up to 300 T by a fast-capacitor of 200 kJ. We have two STC systems, one is a horizontal type (H-type) and the other is a vertical type

	Alias	Type	B _{max}	Pulse width Bore	Power source	Applications	Others
Building C Room 101-113	Electro- Magnetic Flux Compression	destructive	730 T	μ s 10 mm	5 MJ, 40kV	Magneto-Optical Magnetization	5 K – Room temperature
	Horizontal Single-Turn Coil	destructive	300 T 200 T	μ s 5 mm 10 mm	0.2 MJ, 50 kV	Magneto-Optical measurements Magnetization	5 K – 400 K
	Vertical Single-Turn Coil	destructive	300 T 200 T	μ s 5 mm 10 mm	0.2 MJ, 40 kV	Magneto-Optical Magnetization	2 K – Room temperature
Building C Room 114-120	Mid-Pulse Magnet	Non-destructive	60 T	40 ms 18 mm	0.9 MJ, 10 kV	Magneto-Optical measurements Magnetization Magneto-Transport Hall resistance Polarization Magneto-Striction Magneto-Imaging Torque Magneto- Calorimetry Heat Capacity	Independent Experiment in 5 site Lowest temperature 0.1 K
			70 T	40 ms 10 mm			
Building C Room 121	PPMS	Steady State	14 T			Resistance Heat Capacity	Down to 0.3 K
	MPMS	Steady State	7 T			Magnetization	
Building K	Short-Pulse magnet	Non-destructive	87 T (2-stage pulse)	5 ms 10 mm	0.5 MJ, 20 kV	Magnetization Magneto-Transport	2K – Room temperature
			85 T	5 ms 18 mm			
	Long-Pulse magnet	Non-destructive	36 T	1 s 30 mm	210 MJ, 2.7 kV	Resistance Magneto-Calorimetry	2K – Room temperature

Table 1. Available Pulse Magnets, Specifications

(V-type, Fig. 4). Various kinds of laser spectroscopy experiments such as the cyclotron resonance and the Faraday rotation using the H-type STC are available. On the other hand, for very low-temperature experiments, a combination of the V-type STC with a liquid helium bath cryostat is very useful and the magnetization measurements at temperature as low as 2 K can be performed up to 120 T with high precision.

Center of Computational Materials Science

K-computer at Kobe won the title of the world-fastest computer at TOP500 ranking announced at ISC11. Though it is in the 4th place in the list as of today, it is still providing the Japanese scientific community with an incomparable amount of computational resources. With the advancement of hardware and software technologies, large-scale numerical calculations have been making important contributions to materials science and will have even greater impact on the field in the near future. Center of Computational Materials Science (CCMS) is a specialized research center for promoting computer-aided materials science with massively parallel computers, such as K-computer. The center also functions as the headquarters of Computational Materials Science Initiative (CMSI), which is an inter-institutional organization for computational science of a broad range of disciplines, including molecular science, quantum

chemistry, biological materials, and solid state physics. ISSP made contracts with 9 universities and 2 national institutes for supporting the activities of CMSI in which nearly 100 research groups are involved. The main purpose of CMSI is to establish a new community of computational science in which researches from different backgrounds work together on grand challenge problems, thereby developing computational infrastructures (new algorithms, coding styles, standard software packages, etc) and inspire young scientists.

CCMS has a branch office in the RIKEN AICS building on the Port Island Kobe, where K-computer is located, for supporting CMSI researchers getting together at the K-computer site to exchange ideas of computational science, fine-tune various applications software, and develop better contact with staff members of RIKEN, the operating



Fig. 1. CMSI International Satellite Meeting 2013 in Kobe



Fig. 2. Workshop: Programming Techniques for K-Computer (Mishima)

institute of K-computer. Another mission of the Kobe branch of CCMS is exchanging ideas and techniques with researchers from other fields of computer science. (There are 5 major fields in the HPCI strategic program of MEXT, “biology”, “materials and energy” (our field), “seismology, oceanography and meteorology”, “industrial applications”, and “high-energy physics and cosmology”.)

The following is the selected list of meetings organized by CMSI and CCMS in SY2013:

- “CMSI Kobe Hands-On: xTAPP Tutorial” (Apr 23, Jul 30/2013, Kobe)
- “Workshop: Programming Techniques for K-Computer” (Jul 1-Jul 3/2013, Mishima)
- “International Workshop: EQPCM2013” (Jun 3-Jun 21/2013, Kashiwa)
- “CMSI Application Developments Seminar TOKKUN!” (Jun 5, Aug 5, Sep 3/2013, Kobe)
- “CMSI Kobe Hands-On: ALPS Tutorial” (Jul 10, Nov 6/2013, Kobe)
- “CMSI Kashiwa Hands-On: Machikaneyama2002 Tutorial” (Jul 26/2014, Kashiwa)
- “CMSI Division 1 Summer School” (Aug 12-Aug 16/2013, Zao)
- “CMSI Kobe Hands-On: Version Control System Tutorial” (Aug 22/2013, Kobe)
- “CMSI International Satellite Meeting 2013 in Kobe” (Oct 16-Oct 18 /2013, Kobe)
- “CMSI International Satellite Meeting 2013 in Nagoya” (Oct 17-Oct 19 /2013, Nagoya)
- “CMSI International Satellite Meeting 2013 in Tokyo” (Oct 18-Oct 19/2013, Hongo)
- “CMSI International Symposium 2013” (Oct 21-Oct 22/2013, Hongo)
- “CCMS Symposium” (Nov 19-Nov 20/2013, Kashiwa)
- “ISSP supercomputer - CMSI Joint Symposium” (Dec 10-Dec 13/2013, Kashiwa)
- “CMSI Kashiwa Hands-On: Version Control System Tutorial” (Jan 14/2014, Kashiwa)
- “Workshop: Programming Techniques for K-Computer” (Jan 28-Jan 30/2014, Atami)
- “CMSI Kashiwa Hands-On: xTAPP Tutorial” (Feb 26/2014, Kashiwa)
- “Joint Symposium of Elements Strategy Initiative, CMSI, SPring-8, J-PARC and KEK” (Feb 28-Mar 1/2014, Kashiwa)
- “CMSI Kobe Hands-On: Rokko Tutorial” (Mar 11/2014, Kobe)

Laser and Synchrotron Research Center (LASOR Center)

Laser and Synchrotron Research (LASOR) Center started from October, 2012. LASOR Center aims to promote material sciences using advanced photon technologies at ISSP by combining the “Synchrotron Radiation Laboratory” and “Advanced Spectroscopy Group”. These two groups have long histories since 1980’s and have kept strong leaderships in each photon science fields for a long time in the world. In the past several decades, the synchrotron-based and laser-based photon sciences have made remarkable progresses independently. However, recent progresses in both fields make it feasible to merge the synchrotron-based and laser based technologies to develop a new direction of photon and materials sciences. In the LASOR Center, extreme laser technologies such as ultrashort-pulse generation, ultraprecise control of optical pulses in the frequency domain, and high power laser sources for the generation of coherent VUV and SX light are intensively under development. The cutting edge soft X-ray beamline is also developed at the synchrotron facility SPring-8.

LASOR center aims three major spectroscopic methods [ultrafast, ultra-high resolution, and operand spectroscopy] by three groups [extreme laser science group, soft-X-ray spectroscopy and materials science group, and coherent photon science group], as illustrated in Fig.2. Under this framework, various advanced spectroscopy, such as ultra-high resolution photoemission, time-resolved, spin-resolved



Fig. 1. Open ceremony of LASOR center on October 2012.

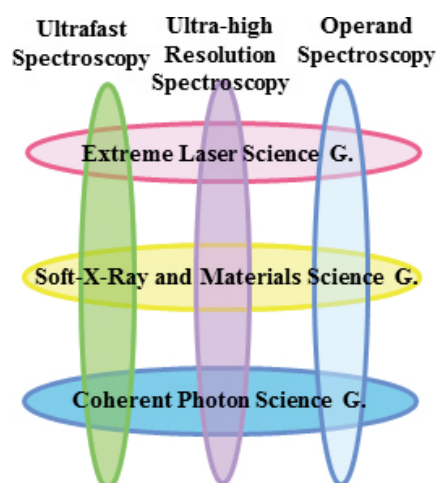


Fig. 2. Developments of advanced spectroscopy at LASOR center by three groups

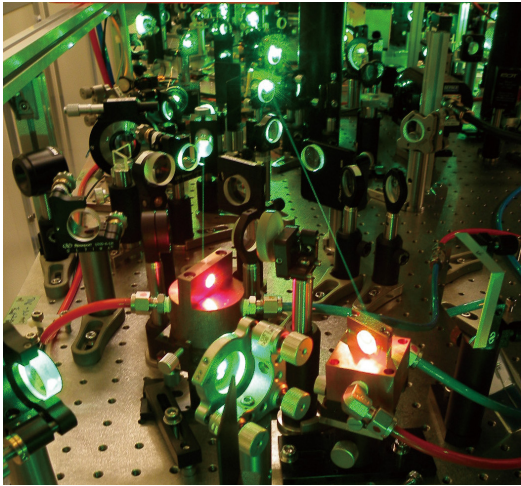


Fig. 3. Close look of a high-peak-power ultrashort-pulse laser

spectroscopy, diffraction, light scattering, imaging, microscopy and fluorescence spectroscopy are in progress by employing new coherent light sources based on laser and synchrotron technologies that cover a wide spectral range from X-ray to terahertz. In LASOR Center, a variety of materials sciences for semiconductors, strongly-correlated materials, molecular materials, surface and interfaces, and bio-materials are studied using advanced light sources and advanced spectroscopy. Another important aim of LASOR Center is the synergy of photon and materials sciences. Most of the research activities on the extreme laser development and their applications to material science are performed in the ISSP buildings D and E at Kashiwa Campus where large clean rooms and the vibration-isolated floor are installed. On the other hand, the experiments utilizing the advanced synchrotron source are performed at beamline BL07 in SPring-8 (Hyogo).

- Extreme Laser Science Group

The advancement of ultrashort-pulse laser technologies in the past decade has transformed the laser development at ISSP into three major directions, (i) towards ultrashort in the time domain, (ii) ultra high resolution in the spectral domain, and (iii) the extension of the spectral range, with extreme controllability of the laser sources. For ultrafast spectroscopy, we have developed carrier-envelope phase stable intense infrared light source that can produce sub-two cycle optical pulses for high harmonic and attosecond pulse generation. So far we observed coherent soft-X-ray radia-

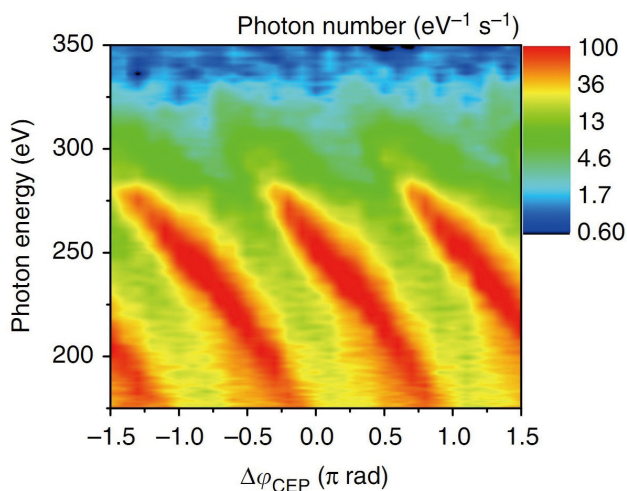


Fig. 4. Phase-dependence of high harmonic spectra in soft X rays.

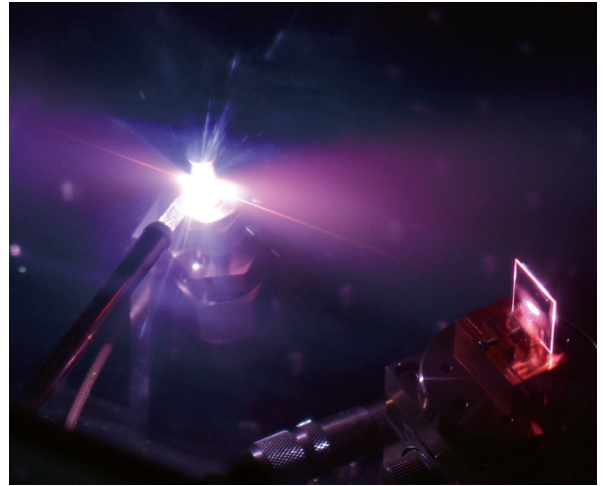


Fig. 5. 10-MHz high harmonic generation in an enhancement cavity.

tion extending to a photon energy of ~ 330 eV. The simulation predicts the soft-X-ray field consists of single isolated attosecond pulses. For ultra-high resolution spectroscopy, fiber-laser-based light sources are intensively developed for producing EUV pulses for high resolution and time-resolved photoemission spectroscopy as well as extending the frequency comb to ultraviolet or infrared for various applications. The spectral range of intense optical pulses are being extended from visible to IR, MIR and THz ranges. Various types of high-repetition-rate ultrastable light sources are developed for laser-based ultrahigh resolution photoemission spectroscopy, high-average-power EUV generation in an enhancement cavity, and frequency comb spectroscopy for atomic physics, astronomical application, and frequency standards.

- Soft-X-ray and Materials Science Group

Recently, VUV and SX lasers have been developed. They become very useful for the materials science, if we develop the SX spectroscopy, such as the cutting-edge photoemission spectroscopy. Laser has a lot of fruitful properties. For examples, by using monochromatic light, ultra-high resolution angle-resolved photoemission spectroscopy (ARPES) is developed. The achieved resolution of $70\text{-}\mu\text{eV}$ is the highest resolution of the world. Fermiology of the materials science with μeV resolution is improved drastically by using the lasers. On the other hand, when we use pulsed laser light, the time resolved ARPES becomes possible. The time resolved photoemission in fs region is powerful to know the relaxation process of photo-induced phase transition. Furthermore, by using CW and circularly light in VUV region, the photoelec-

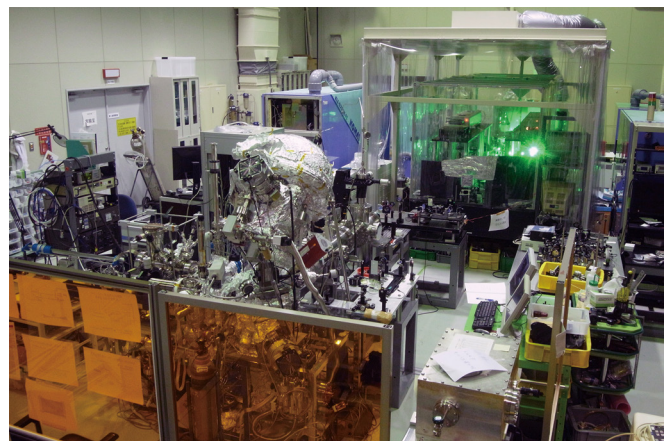


Fig. 6. Pump-probed photoemission system using 60-eV laser

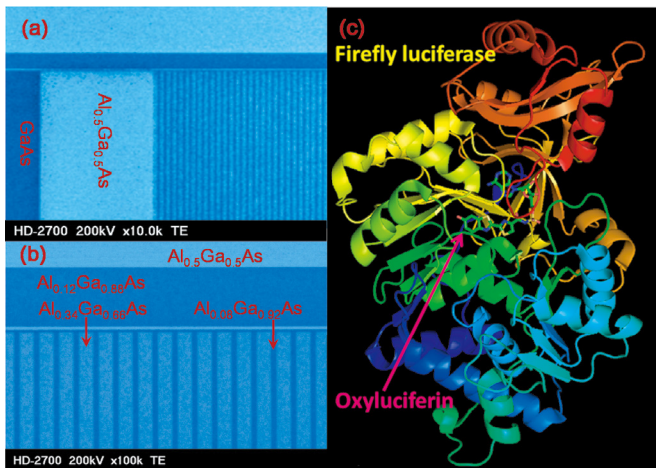


Fig. 7. Photonics devices under study: (left panel) semiconductor quantum wires and (right panel) firefly-bioluminescence system consisting of light emitter (oxyluciferin) and enzyme (luciferase)

tron microscopy (PEEM) is developed. The spatial resolution of nm region is very powerful for the nanomaterials.

- Coherent Photon Science Group

The coherent-photon science group has main interests in exploring a variety of coherent phenomena and non-equilibrium properties of excited states in condensed matters, in collaborations with research groups in charge of photoemission, operand-spectroscopy and extreme laser science. This group covers a wide range of materials, from semiconductors, ferromagnets, complexes and superconductors to biomaterials. Various ultrafast optics technologies such as femtosecond luminescence and pump-and-probe transmission/reflection spectroscopy are applied to studies on wavepacket dynamics, photo-induced phase transitions and carrier dynamics. Coherent control and observation of spin dynamics in magnetic materials and metamaterial structures by using high power terahertz radiation source is extensively studied. Advanced photonics devices are intensively studied, such as quantum nano-structure lasers with novel low-dimensional gain physics, low-power light-standard LEDs, very efficient multi-junction tandem solar cells for satellite use, and wonderful bio-/chemi-luminescent systems for wide bio-technology applications.

Synchrotron Radiation Laboratory

The Synchrotron Radiation Laboratory (SRL) was established in 1975 as a research division dedicated to solid state physics using synchrotron radiation (SR). In 1989, SRL started to hold the Tsukuba branch, in the Photon Factory (PF), High Energy Accelerator Research Organization (KEK). SRL maintains a Revolver undulator, two beamlines and three experimental stations; BL-18A for angle-resolved photoemission spectroscopy with SCIENTA electron analyzer, while undulator beamline BL-19A and BL-19B, for spin- and angle-resolved photoelectron spectroscopy (SARPES) and soft X-ray emission spectroscopy experiments, respectively. Recently, a high-yield spin detector, using very low energy electron diffraction, was developed at BL-19A. SARPES measurements have now been performed with high-resolution and the experiments at the beamline have become important for exciting topics of surface/solid state physics such as topological insulators and ferromag-



Fig. 1. 3D nano ESCA at SPring-8 BL07LSU

netic nanofilms.

The SRL staffs have joined the Materials Research Division of the Synchrotron Radiation Research Organization (SRRO) of the University of Tokyo and they have played an essential role in constructing a new high brilliant soft X-ray beamline, BL07LSU, in SPring-8. The light source is the polarization-controlled 25-m long soft X-ray undulator. The monochromator is equipped with a varied-line-spacing plain grating, which covers the photon energy range from 250 eV to 2 keV. At the downstream of the beamline, four experimental stations have been developed for frontier spectroscopy researches: the three-dimensional (3D)



Fig. 2. XES station at SPring-8 BL07LSU

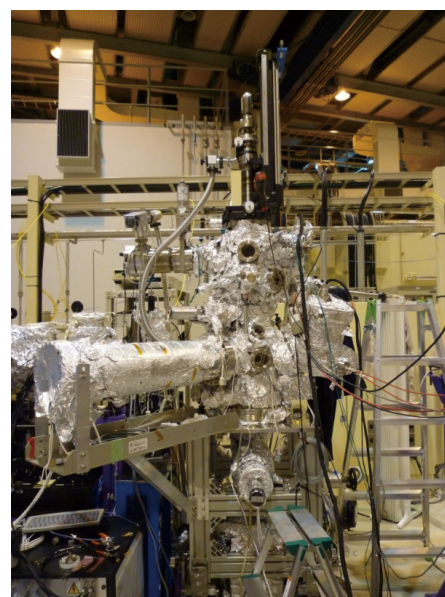


Fig. 3. TR-SX station at SPring-8 BL07LSU

nano-ESCA station, the soft X-ray emission spectroscopy (XES) station, the time-resolved soft X-ray spectroscopy (TR-SX) station, and the free-port station for any experimental apparatus. The beamline construction was completed in 2009 and SRL established the Harima branch laboratory in SPring-8. At SPring-8 BL07LSU, each end-station has achieved high performance: the 3D nano-ESCA reaches the spatial resolution of 70 nm, the XES station obtains spectra with energy resolving power $E/\Delta E$ larger than 5,000, and the TR-SX have established the laser-pump and SR-probe method with the time-resolution of 50 ps which corresponds to the SR pulse-width. The four end-stations have now been opened fully to outside users. In 2013, 153 researchers made their experiments during the SPring-8 operation time of 3400 hours.

Experimental Realization of a Quantum Breathing Pyrochlore Antiferromagnet

K. Kimura and S. Nakatsuji

Exploring novel and exotic phenomena associated with spin degrees of freedom has been central subject in condensed matter physics [1]. One of the most attractive systems in three dimension is a pyrochlore lattice magnet, which consists of corner-sharing regular tetrahedra of magnetic ions. The inherent geometrical frustration suppressing a conventional magnetic order often leads to a variety of unusual properties [1]. A key building unit of pyrochlore magnets is a single spin tetrahedron. Besides being a good starting point for considering the essence of physics of full pyrochlore lattice, it has been theoretically shown to possess interesting properties such as a doubly degenerate singlet state which can be labelled by scalar spin chirality [2]. To our knowledge, however, there has been no experimental realization of the $S = 1/2$ quantum spin tetrahedral system, partly because typical $3d$ transition metal ions with $S = 1/2$ (like Cu^{2+}) are difficult to keep the tetrahedral symmetry due to the inherent Jahn-Teller instability.

Here, we report the new Yb-based quantum spin system $\text{Ba}_3\text{Yb}_2\text{Zn}_5\text{O}_{11}$ [3]. Polycrystalline samples were synthesized by the standard solid state reaction method. The Rietveld refinement on powder X-ray diffraction pattern has revealed that this material crystallizes into the cubic structure with space group $F\bar{4}3m$, and Yb^{3+} ions form a so-called breathing pyrochlore lattice [4] characterized by an alternating array of small and large Yb^{3+} regular tetrahedra (Fig. 1(a), inset). Analyses of the crystalline electric field (CEF) scheme of Yb^{3+} ions ($4f^{13}$) and magnetic susceptibility data down to 30 K show that the CEF ground state is approximated by a magnetic Kramers doublet with the isotropic effective g -factor $g_{\text{eff}} = 2.66$ for pseudospin-1/2. The very large gap (>500 K) to the excited states ensures that the low-temperature properties are described by pseudospin-1/2.

The temperature dependence of the magnetic susceptibility below 30 K is shown in Fig. 1(a). A broad maximum at around 4 K suggests a formation of a quantum spin singlet state due to antiferromagnetic interactions in a small Yb tetrahedron. This is supported by the magnetization curves at selected temperatures (Fig. 1(b)). Though linear above 4 K, the magnetization curves show a clear non-linear increase at $B \sim 3$ T below 4 K, a signature of the singlet-triplet crossover. These results are analyzed based on the pseudospin-1/2 single tetrahedron model with Heisenberg interactions J . The good agreement is obtained with $J = -6.43$ K and $g_{\text{eff}} = 2.569$, as indicated by the solid lines in Figs. 1(a) and 1(b), suggesting a formation of the doubly degenerate singlet state

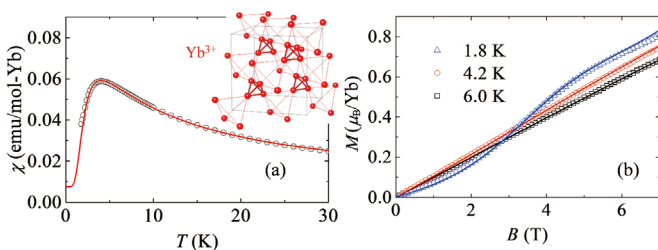


Fig. 1. (a) The temperature dependence of the magnetic susceptibility below 30 K. Inset: Breathing pyrochlore lattice formed by Yb ions. (b) The magnetization curves at selected temperatures. Solid lines in (a) and (b) represent calculated values based on the single tetrahedron model with Heisenberg $J = -6.43$ K and $g_{\text{eff}} = 2.569$.

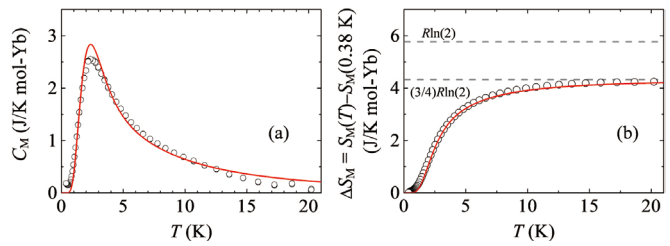


Fig. 2. The temperature dependence of (a) the magnetic specific heat C_M and (b) corresponding magnetic entropy S_M . Solid lines in (a) and (b) are fit to the single tetrahedron model. The dashed lines in (b) denote the entropy for a two level system $R\ln(2)$ and for a doubly degenerate singlet state $(3/4)R\ln(2)$.

with chirality fluctuations predicted by the model [2]. Solid evidence for the double degeneracy is provided by magnetic specific heat C_M measured at ISSP (Fig. 2(a)). C_M down to 0.38 K exhibits a broad peak associated with the singlet formation without any signs of long-range order. Corresponding magnetic entropy S_M is shown in Fig. 2(b). The saturated value at 20 K is close to 75% of the value expected for a standard two level system $R\ln(2)$, and 25% of magnetic entropy remains below 0.38 K. This value is fully consistent with the doublet degeneracy of the singlet state expected from the single tetrahedral model. Moreover, as indicated by the red line of Figs. 2(a) and 2(b), C_M and S_M are well reproduced by the model.

All the data presented in this study therefore uncover the unique doubly degenerate singlet state with chirality fluctuations at $T = 0.38$ K. To the best of our knowledge, this is a new quantum state of matter which has never been established in existing materials. The mechanism for the lifting of the degeneracy is highly interesting and left for the future study.

References

- [1] L. Balents, Nature **464**, 199 (2010).
- [2] H. Tsunetsugu, J. Phys. Soc. Jpn. **70**, 640 (2001).
- [3] K. Kimura, S. Nakatsuji, and T. Kimura, arXiv: 1404.6439
- [4] Y. Okamoto, G. J. Nilsen, J. P. Attfield, and Z. Hiroi, Phys. Rev. Lett. **110**, 097203 (2013).

Authors

K. Kimura^a, S. Nakatsuji, and T. Kimura^a
^aOsaka University

Entanglement Spectra between Coupled Tomonaga-Luttinger Liquids

R. Lundgren, Y. Fuji, and S. Furukawa

Quantum entanglement has emerged as a new tool to characterize quantum phases. While the entanglement is nothing but “quantum correlation” that has been a central issue in condensed matter physics for a long time, new quantitative descriptions of the entanglement stimulated by quantum information theory have proved useful. The most frequently used quantity to describe the entanglement in quantum many-body problem is “entanglement entropy”. However, there are other quantities which can be useful, and entanglement spectrum is one of them. Its relation to the spectrum of physical edge states is conjectured [1], and has been confirmed in several examples.

Here we report on a recent joint research [2] on entanglement spectra between two coupled Tomonaga-Luttinger

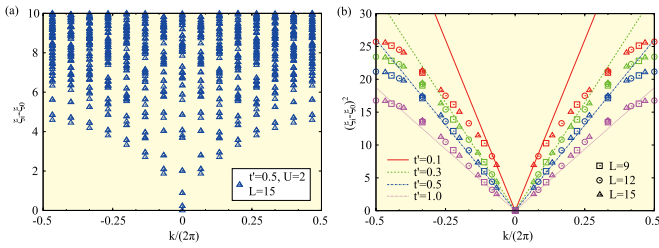


Fig. 1. The dispersion of entanglement spectra of a spin ladder model when a linear combination of two TL fields remains gapless while the other acquires a gap. The numerically obtained dispersion relation agrees well with the peculiar square-root dependence predicted by the theory.

liquids (TLLs). TLL is a ubiquitous effective field theory for quantum many-body problem in one dimension, and many physical systems such as quantum spin ladders and carbon nanotubes are described as coupled TLLs. There are variety of phases in coupled TLLs. In a class of gapless phases of coupled non-chiral TLLs, we find an entanglement spectrum with a dispersion relation proportional to the square root of the subsystem momentum. This result was derived using the field theory, and was then confirmed numerically for a spin ladder model. Such a dispersion is generally not expected for a spectrum of physical excitations, including those of edge states. We relate the unusual dispersion relation in the entanglement spectrum to a long-range interaction in the entanglement Hamiltonian. Our result sheds new light on the correspondence between the entanglement spectrum and the spectrum of the edge states.

This work was performed during a visit by R. Lundgren, a Ph. D. student at University of Texas, under the NSF East Asia and Pacific Summer Institutes for U.S. Graduate Students and the JSPS Summer Program, hosted by ISSP in cooperation with Department of Physics, the University of Tokyo.

References

- [1] H. Li and F. D. M. Haldane, Phys. Rev. Lett. **101**, 010504 (2008).
 [2] R. Lundgren, Y. Fuji, S. Furukawa, and M. Oshikawa, Phys. Rev. B **88**, 245137 (2013).

Authors

R. Lundgren^a, Y. Fuji, S. Furukawa^b, and M. Oshikawa^a
^aUniversity of Texas at Austin
^bThe University of Tokyo

Robust Protection from Backscattering in a Topological Insulator

Y. Ando, S. Shin and F. Komori

Surface of three-dimensional (3D) topological insulators (TIs) is a promising platform for novel device functions, whereon robust spin-polarized surface states occur due to topological feature of the bulk wave functions. High carrier mobility is expected on 3D TI surface because 180° backscattering is forbidden under the spin-helical texture of the topological surface states (TSSs). However, the prohibition range of backscattering has not been clarified yet. Here, we study how the elastic scattering is suppressed as functions of the scattering angle and electron energy in a single and unwarped upper Dirac cone of Bi_{1.5}Sb_{0.5}Te_{1.7}Se_{1.3} [1]. The quaternary compound Bi_{1.5}Sb_{0.5}Te_{1.7}Se_{1.3} is identified to a bulk-insulating TI, whose transport properties are dominated

by the surface [2], and thus is suitable for investigating the TSS characteristics.

The elastic-scattering vector within the TSS on the cleaved surface was obtained from a quasiparticle interference (QPI) pattern, which is a Fourier-transformed constant-voltage dI/dV image measured using scanning tunneling microscopy at 5 K (Fig. 1). The observed elastic scattering amplitude within the TSS was critically suppressed beyond certain scattering-vector lengths, both in the $\bar{\Gamma}$ - \bar{M} and in $\bar{\Gamma}$ - \bar{K} directions. That is, there is a critical scattering-vector length,

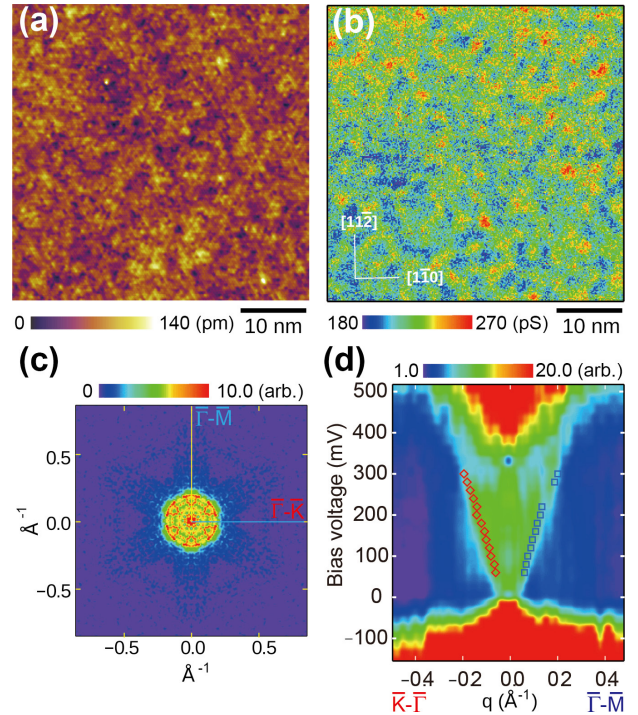


Fig. 1. (a) Topographic STM image of a cleaved surface of Bi_{1.5}Sb_{0.5}Te_{1.7}Se_{1.3}. (b) dI/dV image at the sample bias voltage $V_b = 0.28$ V. (c) Amplitude map of the elastic scatterings, or QPI map, derived by Fourier transformation (FT) of the dI/dV image shown in (b). (d) FT amplitude image in $\bar{\Gamma}$ - \bar{K} and in $\bar{\Gamma}$ - \bar{M} directions as functions of V_b . Critical scattering-vector lengths are plotted as red and blue symbols.

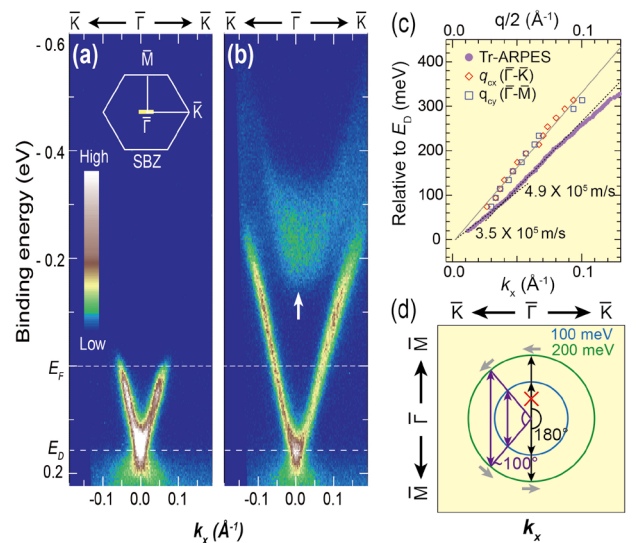


Fig. 2. (a,b) Intensity maps of ARPES before (a) and after (b) impinging a 170-fs pump laser pulse (1.5 eV). The dispersions above E_F are revealed by pumping the electrons into the unoccupied side. An arrow in (b) indicates the bottom of the bulk conduction band. (c) Comparison between critical scattering-vector lengths q_{cx} and q_{cy} (red and blue symbols) obtained from QPI images and the dispersion of the TSS (circles) from pump-probe ARPES. (d) Schematic of the elastic scattering within a nearly ideal Dirac TSS. Scattering angle larger than 100° is effectively prohibited.

qc, beyond which the scattering is effectively prohibited. The critical length increased with the increase of energy from the Dirac point as shown in Fig. 1(d). The band dispersions displayed in Fig. 2(a,b) were recorded by using angle-resolved photoemission spectroscopy (ARPES) implemented by a pump-and-probe method. Here, the dispersions above the Fermi level were revealed by pumping electrons into the unoccupied states (Fig. 2(b)). A nearly ideal Dirac-cone dispersion was observed within the bulk band gap. The locus of the Dirac point, bulk-conduction-band minimum, and the band velocity of the TSS were obtained. We find that the critical scattering vector length is 75 % shorter than the length of the 180° backscattering vector (Fig. 2(c)). This indicates that the scattering in the TSS is effectively prohibited in a wide angular range of $100\text{--}180^\circ$ as schematically shown in Fig. 2(d). The robust protection from backscattering is good news for applications, but it poses a challenge to the theoretical understanding of the transport in the TSS.

References

- [1] S. Kim, *et al.*, *Phys. Rev. Lett.* **112**, 136802 (2014).
 [2] A. A. Taskin *et al.*, *Phys. Rev. Lett.* **109**, 066803 (2012).

Authors

S. Kim, S. Yoshizawa, Y. Ishida, K. Eto^a, K. Segawa^a, Y. Ando^a, S. Shin, and F. Komori^a
^aOsaka University

Microscopic Origin of π Electronic States in Silicene Revealed by Scanning Tunneling Microscopy

Y. Yamada-Takamura, T. Ozaki, and Y. Hasegawa

Silicene, a monolayer of silicon atoms forming a two-dimensional honeycomb lattice, has attracted significant attention in condensed matter physics because it has electronic states similar with its carbon counterpart, graphene and shares almost all the remarkable properties of graphene [1], such as massless Dirac fermion, pseudo spin, and the K/K' valleys. There are, however, some differences between the two ultimately thin materials; while graphene has a planar structure, silicene is buckled [1]; the atoms in the two sub-lattices have different heights, providing us a possibility of inducing a staggered potential by an application of an external electrical field [2]. Different from graphene, silicene exhibits significant spin-orbit coupling [3], making it bear topologically nontrivial electronic structure, which realizes the quantum spin Hall effect or two-dimensional topological insulator. The staggered potential can lift up degeneracy of the K and K' valleys, opening up a possibility of an effective spin polarized electron source [4].

Silicene has been formed so far on metal substrates, such as Ag [5-7] by depositing Si on the substrate. It can also be formed epitaxially on ZrB_2 thin film grown on Si(111) substrate [8]; by annealing silicon atoms segregate from the substrate to form the one-monolayer silicon thin film on the $\text{ZrB}_2(0001)$. Because of the lattice matching between the 2×2 unit cell of $\text{ZrB}_2(0001)$ and the $\sqrt{3} \times \sqrt{3}$ unit cell of silicene, the silicene on ZrB_2 exhibits a $\sqrt{3} \times \sqrt{3}$ reconstruction. Using a low-temperature scanning tunneling microscopy and spectroscopy (STM/STS), we investigated atomic and electronic structures of the silicon layer [9]. By comparing the experimental results with those of first-principles density functional theory calculations, we determined the atomic

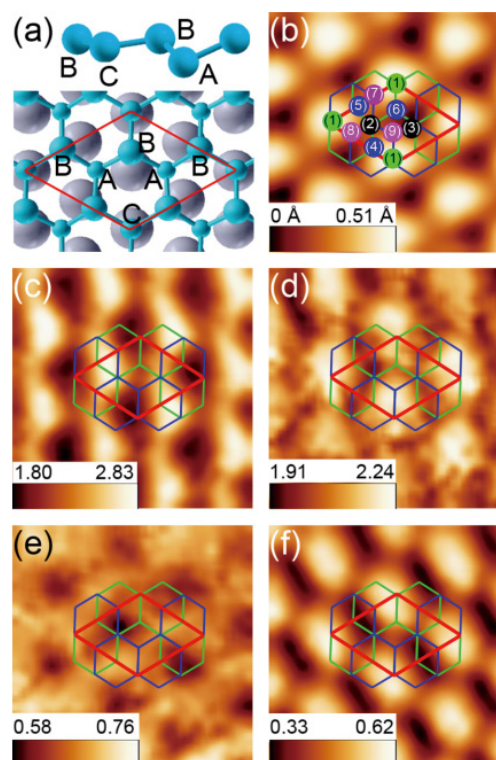


Fig. 1. (a) atomic structure of epitaxial silicene on $\text{ZrB}_2(0001)$ derived from DFT calculations. Si atoms are colored in blue and Zr atoms are colored in grey. (b) STM image ($2 \text{ nm} \times 2 \text{ nm}$) (c-f) tunneling conductance (dI/dV) images taken at the sample bias voltages of -0.47 V , -0.36 V , and -0.12 V , respectively.

structure and discussed the electronic states and the bonding nature of each Si atoms within the unit cell.

Figure 1 shows results taken by STM/STS. Figure 1(a) is an atomic structural model determined in the present study. Figure 1(b) is an STM image, and (c-f) are tunneling conductance (dI/dV) images taken at various bias voltages, that is, local density of states (LDOS) mappings at the corresponding energy level with respect to the Fermi energy.

The structural model (Fig. 1(a)) and the STM image (b) indicate that the protrusions observed in the STM image come from the atoms, marked C in the schematic, sitting on top of Zr atoms. Because of the local configuration, the buckling of the atom C is suppressed, making its orbitals hybridize in planar sp_2 manner. The tunneling spectra taken on the atoms indicate significant contribution of the p_z orbital to π/π^* valence/conduction bands, which was observed with angle-resolved photoemission (ARPES) [10]. The STS results also confirm the band gap due to the $\sqrt{3} \times \sqrt{3}$ buckled reconstruction observed by the ARPES study. On the other hand, atom A, which belongs to the same sub-lattice as atom C, exhibits buckling larger than the free-standing silicene, and possesses sp_3 -like hybridized orbitals. The STM/STS results evidenced a clear correlation between hybridization of the orbitals of the Si atoms and the buckling.

References

- [1] S. Cahangirov, M. Topsakal, E. Akturk, H. Sahin, and S. Ciraci, *Phys. Rev. Lett.* **102**, 236804 (2009).
 [2] M. Ezawa, *New J. Phys.* **14**, 033003 (2012).
 [3] C.-C. Liu, W. Feng, and Y. Yao, *Phys. Rev. Lett.* **107**, 076802 (2011).
 [4] W.-F. Tsai, C.-Y. Huang, T.-R. Chang, H. Lin, H.-T. Jeng, and A. Bansil, *Nat. Commun.* **4**, 1500 (2013).
 [5] P. Vogt, P. De Padova, C. Quaresima, J. Avila, E. Frantzeskakis, M. C. Asensio, A. Resta, B. Ealet, and G. Le Lay, *Phys. Rev. Lett.* **108**, 155501 (2012).
 [6] L. Chen, C.-C. Liu, B. Feng, X. He, P. Cheng, Z. Ding, S. Meng, Y. Yao, and K. Wu, *Phys. Rev. Lett.* **109**, 056804 (2012).

- [7] C.-L. Lin, R. Arafune, K. Kawahara, N. Tsukahara, E. Minamitani, Y. Kim, N. Takagi, and M. Kawai, *Appl. Phys. Express* **5**, 045802 (2012).
- [8] A. Fleurence, R. Friedlein, T. Ozaki, H. Kawai, Y. Wang, and Y. Yamada-Takamura, *Phys. Rev. Lett.* **108**, 245501 (2012).
- [9] A. Fleurence, Y. Yoshida, C.-C. Lee, T. Ozaki, Y. Yamada-Takamura, and Y. Hasegawa, *Appl. Phys. Lett.* **104**, 021605 (2014).
- [10] R. Friedlein, A. Fleurence, J. T. Sadowski, and Y. Yamada-Takamura, *Appl. Phys. Lett.* **102**, 221603 (2013).

Authors

A. Fleurence^a, Y. Yoshida, C.-C. Lee^a, T. Ozaki^a, Y. Yamada-Takamura^a, and Y. Hasegawa^a
^aJapan Advanced Institute of Science and Technology

Multiferroic Nanopillar Composites

Y. Matsumoto and M. Lippmaa

Composite materials can be used to elastically couple ferroelectrics and ferromagnets, producing a multiferroic material where the magnetization can be controlled by an electric field or the dielectric polarization by a magnetic field. In this work, a nanoscale pillar-and-matrix composite, consisting of a layered $\text{Bi}_5\text{Ti}_3\text{FeO}_{15}$ (BTFO) perovskite matrix and nanoscale pillars of a ferrimagnetic spinel CoFe_2O_4 (CFO), were used to study the effectiveness of nanoscale strain-mediated elastic coupling. The main advantage of this approach is that it may be possible to develop new types of multiferroics that can work close to room temperature and do not contain lead.

A three-dimensional model of the composite material is shown in Fig. 1(b), together with a surface electron microscope image in Fig. 1(a). The pillars form spontaneously during thin film growth due to immiscibility of the perovskite and spinel phases and extend throughout the thickness of the thin film, as shown in the cross-sectional transmission electron microscope image in Fig. 1c. Composition mapping shows nearly perfect segregation of Fe/Co and Bi/Ti in pillars with an average diameter of about 50 nm.

From the point of view of achieving elastic multiferroic coupling in a nanoscale composite, strain fields along the walls of the nanopillars are critically important. The behavior was analyzed by high-resolution electron microscopy, which showed that the nanostructure-matrix interface is heavily strained. The strain relaxes gradually in the BTFO matrix,

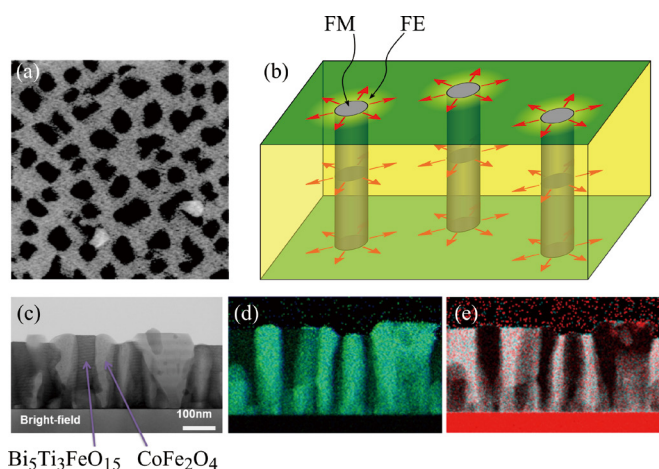


Fig. 1. (a) Scanning electron microscope image of the nanocomposite film surface and (b) a three-dimensional model of the composite material. The elastic strain field surrounding the nanopillars is marked with red arrows. (c) Cross-sectional electron microscope image and (d) Co/Fe and (e) Bi/Ti EDS mapping images.

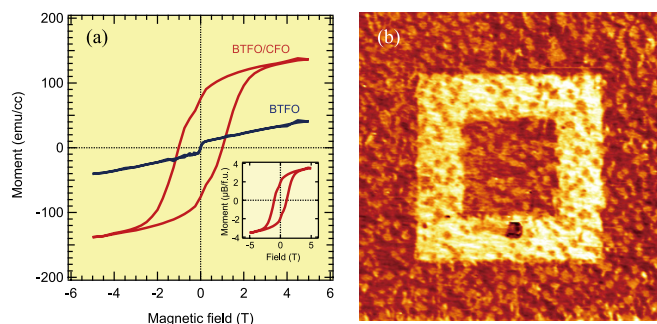


Fig. 2. (a) Magnetization comparison of a pure BTFO matrix and the BTFO/CFO nanocomposite film, showing the presence of ferromagnetism in the nanopillars. Inset shows the magnetization of a pure CFO sample. (b) A ferroelectrically poled pattern on the surface of a nanocomposite film, measured with a piezoresponse force microscope.

as illustrated by the red radial arrows in Fig. 1(b). Ferroelectric switching in the BTFO matrix material was studied by piezoresponse force microscopy, showing that the polarization response depends on the volume fraction of nanopillars, reaching a maximum for a CFO volume of 35%. A bipolar poling pattern for this sample is shown in Fig. 2(b). Analysis showed the presence of both in-plane (ab plane) and out-of-plane (c -axis) polarization components, which is unusual for layered bismuth perovskite ferroelectrics where the polarization direction is in the ab plane. Thermodynamic Landau-Ginzburg-Devonshire (LGD) calculations showed that this is a direct result of the strain fields surrounding the nanopillars and may also be caused by the presence of shear domains at pillar boundaries that are not perfectly c -axis oriented. Magnetization analysis of the composites at 10 K showed that the saturation magnetization of CFO is not significantly affected by the 50 nm diameter of the nanopillars (Fig. 2a), reaching nearly the expected $4 \mu_B/\text{f.u.}$ of bulk CFO.

The work showed that systematic strain control is possible in spontaneously-formed nanopillar composites consisting of a spinel ferromagnet and a perovskite ferroelectric. The piezoresponse analysis showed that the three-dimensional nanoscale structuring and the associated strain fields are critical for obtaining suitable polarization behavior in the layered bismuth ferroelectrics. Work is now underway to determine the multiferroic response in such nanocomposite systems.

Reference

- [1] A. Imai, X. Cheng, H. L. Xin, E. A. Eliseev, A. N. Morozovska, S. V. Kalinin, R. Takahashi, M. Lippmaa, Y. Matsumoto, and V. Nagarajan, *ACS Nano* **7**, 11079 (2013).

Authors

A. Imai^{a,b}, X. Cheng^b, H. L. Xin^c, E. A. Eliseev^d, A. N. Morozovska^d, S. V. Kalinin^c, R. Takahashi, M. Lippmaa, Y. Matsumoto^f, and V. Nagarajan^b
^aTokyo Institute of Technology
^bUniversity of New South Wales
^cBrookhaven National Laboratory
^dNational Academy of Sciences of Ukraine
^eOak Ridge National Laboratory
^fTohoku University

Development of High Pressure, High Field and Multi-Frequency ESR System Using Hybrid Type Pressure Cell

T. Sakurai, H. Ohta, and Y. Uwatoko

Pressure has been recognized as one of the most important parameters to explore novel phenomena around the quantum critical point for quantum spin systems. As the high field and multi-frequency ESR is a powerful means to study quantum spin systems from the microscopic point of view, it is very useful to introduce the parameter of pressure to the ESR measurement. We developed the high pressure, high field and multi-frequency ESR apparatus by combining the single-pass transmission type ESR apparatus using the pulsed high magnetic field up to 55 T and the unique piston cylinder pressure cell previously [1]. The most characteristic feature of this pressure cell is that all inner parts are made of zirconium oxide which has relatively good transmittance of electromagnetic wave. It enables us to observe ESR under pressure. However, the pressure range is limited below 1 GPa at most because the single layer cylinder is used and its inner and outer diameters are 3 and 8 mm, respectively. The limited sample space also affects the signal intensity. The signal to noise ratio is not enough to study spin states in detail. Moreover, several compounds have been suggested to have the critical pressures above 2 GPa recently [2]. Therefore, the new ESR apparatus which has higher pressure range and sensitivity is required. In this study, we have developed new ESR apparatus which uses the combination of the hybrid type pressure cell and the superconducting magnet to improve these two points [3].

Figure 1 shows the newly developed pressure cell for multi-frequency ESR measurement. The hybrid type cylinder which consists of inner NiCrAl cylinder and outer CuBe sleeve is used to achieve both larger sample space and higher pressure range above 2 GPa. The inner and outer diameters of the cylinder are 5 and 28 mm, respectively. The inner parts are all made of zirconium oxide. We confirmed that the pressure can be generated over 2.5 GPa at low temperature. However, they are sometimes cracked when the load is applied to generate the pressure over 2.5 GPa at low temperature. We have also developed new ESR apparatus using cryogen free superconducting magnet with wide bore. Gunn oscillator and backward wave oscillator which cover the frequency region from 50 to 400 GHz are used as the light source. The ESR signal is detected by an InSb detector and

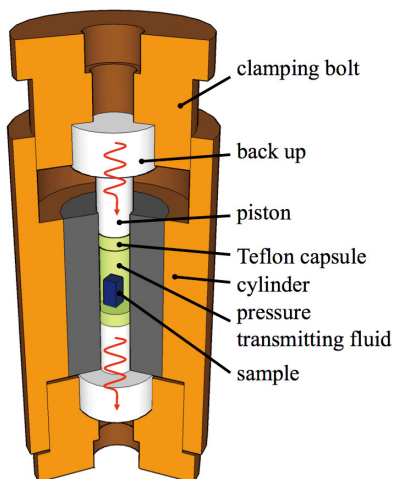


Fig. 1. Cut view of the hybrid type pressure cell for multi-frequency ESR measurement. Red lines show the electromagnetic wave.

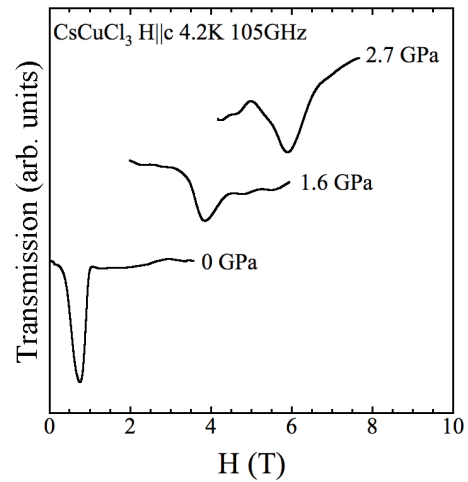


Fig. 2. Pressure dependence ESR spectra of CsCuCl₃ for H||c at 105 GHz.

the signal is amplified by the lock-in technique. The larger sample space and the use of the lock-in technique make the sensitivity higher than previous apparatus successfully. Figure 2 shows typical ESR spectra obtained by the developed high pressure ESR apparatus. CsCuCl₃ is a well known ABX₃ type antiferromagnet with $T_N = 11$ K. Figure 2 shows the antiferromagnetic resonance of this compound obtained at 4.2 K for H||c. It clearly shows that the resonance field shifts to the higher field side as the pressure is increased. This corresponds to the increase of the antiferromagnetic gap on applying the pressure [4]. The maximum pressure obtained in this measurement is 2.7 GPa as shown in Fig. 2. This result also shows that this high pressure ESR apparatus is promising tool to clarify the spin states of novel pressure induced phenomenon for quantum spin system.

References

- [1] T. Sakurai *et al.*, Rev. Sci. Instrum. **78**, 065107 (2007).
- [2] T. Sakurai *et al.*, J. Phys. Conf. Ser. **150**, 042171 (2009).
- [3] K. Fujimoto *et al.*, Appl. Magn. Reson. **44**, 893 (2013).
- [4] T. Sakurai *et al.*, J. Phys. Conf. Ser. **215**, 012184 (2010).

Author

T. Sakurai^a, S. Okubo^a, H. Ohta^a, K. Matsubayashi, and Y. Uwatoko^a
^aKobe University

One-Hundred-Million-Atom Electronic Structure Calculations on the K Computer

T. Hoshi

In the current (peta-scale) or next generation (exa-scale) computational physics, a crucial issue is ‘Application-Algorithm-Architecture co-design’ or inter-disciplinary collaborations among physics, applied mathematics and the high-performance computation field.

Here we report that one-hundred-million atom (100-nm-scale) electronic structure calculations were realized on the K computer [1,2]. The methodologies were based on the co-design. In particular, the novel iterative (Krylov-subspace) algorithms were constructed for the generalized shifted linear equations $((zS-H)x=b)$, instead of the conventional generalized eigen-value equation $(Hy=eSy)$ (See [3,4] and reference therein). The methods give the real-space Green’s function, instead of eigen states. These solvers were implemented in our order- N calculation code ELSESES (<http://www.elses.jp/>) with modeled (tight-binding) systems based on *ab initio*

calculations. These solver algorithms are purely mathematical and applicable to large-matrix problems in many computational physics fields beyond electronic structure calculations.

In Fig. 1, the calculations show high parallel efficiency ('strong scaling') with up to the full core calculations of the K computer for one-hundred-million-atom (100-nm-scale) systems [1,2]. The calculated systems are amorphous-like conjugated polymer (aCP), poly-(9,9 dioctyl-fluorene) with $N=102,238,848$ atoms and sp^2 - sp^3 nano-composite carbon solid (NCCS) with $N=103,219,200$ atoms. The high parallel efficiency stems not only from the fundamental mathematical theory but also from detailed techniques, such as programing techniques for saving memory and communication costs and a parallel file I/O [4].

An application study with NCCS is picked out [4]. The study is an early-stage one on the formation process of the nano-polycrystalline diamond (NPD), a novel ultra-hard material [5]. NPD is obtained by direct conversion sintering process from graphite under high pressure and high temperature and has characteristic 10-nm-scale lamellar-like structures. NPD is of industrial importance for its extreme hardness and strength and Sumitomo Electric Industries. Ltd. began commercial production from 2012. Our simulation is motivated by the investigation of possible precursor structures in the formation process of NPD and the structures should be nano-scale composites of sp^2 (graphite-like)

and sp^3 (diamond-like) domains. Figure 2 shows the nano-domain analysis on the NCCS. The structure is a result of our simulation. The π -type crystalline orbital Hamiltonian population (π COHP) analysis [4], an analysis method based on the Green's function, was used so as to distinguish the sp^2 and sp^3 domains. The analysis clarifies shapes of domains and structure of domain boundaries from huge electronic structure data and gives theoretical foundations of the composite.

General future aspects are (i) large-scale calculation methods for optical and transport properties and (ii) applications to various systems, such as organic materials.

The fundamental mathematical theory was constructed in the collaboration with applied mathematics researchers; T. Sogabe (Aichi Prefectural University) and S.-L. Zhang (Nagoya University) [3]. The code for massive parallelism was developed with the supercomputers, the systems B and C, at ISSP and the K computer was used in the research proposals of hp120170, hp120280 and hp130052.

References

- [1] T. Hoshi *et al.*, JPS Conf. Proc. **1**, 016004 (2014).
- [2] T. Hoshi *et al.*, Proceedings of Science, in press (Preprint : <http://arxiv.org/abs/1402.7285/>)
- [3] T. Hoshi *et al.*, J. Phys.: Condens. Matter **21**, 165502 (2012).
- [4] T. Hoshi *et al.*, J. Phys. Soc. Jpn. **82**, 023710 (2013).
- [5] T. Irifune *et al.*, Nature **421**, 599 (2003).

Author
T. Hoshi^{a,b}
^aTottori University
^bJST-CREST

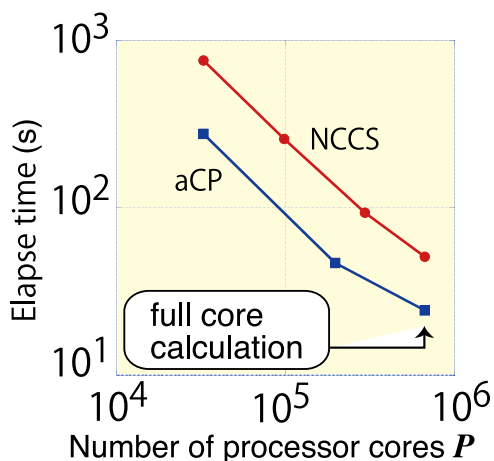


Fig. 1. Benchmark for the parallel efficiency ('strong scaling') on the K computer with one hundred million atoms. [1,2] The calculated systems are amorphous-like conjugated polymer (aCP), poly-(9,9 dioctyl-fluorene) and sp^2 - sp^3 nano-composite carbon solid (NCCS).

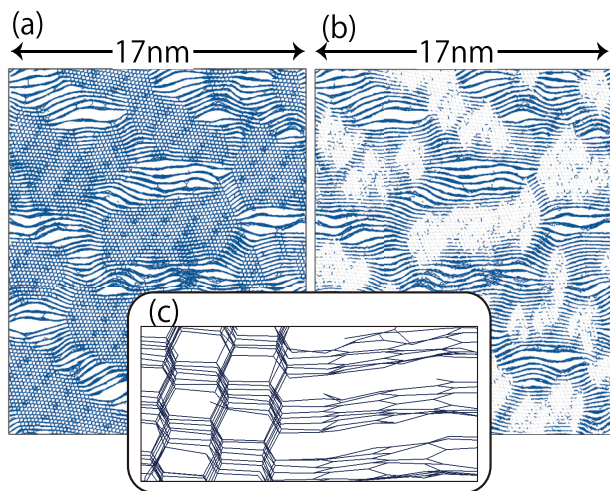


Fig. 2. Nano-domain analysis of NCCS visualized with the π COHP [4]. The sp^2 (graphite-like) and sp^3 (diamond-like) domains are visualized in (a), while only the sp^2 domains are visualized in (b). A closeup of an sp^2 - sp^3 domain boundary is shown in (c).

Rolled Lamellar Structure of Surfactant Membranes Induced by Shear Flow

H. Shiba, H. Noguchi, and G. Gompper

Surfactant molecules in water self-assemble into various structures such as micelles and bilayer membranes, which display a rich variety of rheological properties. It is known that under shear flow, lamellar membranes can be oriented parallel or perpendicular to the shear-gradient direction. Surprisingly, under high shear flow, the membranes transform the planar lamellae to a closely-packed multi-lamellar vesicle structures, so-called the onion phase. The onion radius is reversible and can be described by a unique decreasing function of the shear rate. Although this onion phase was experimentally discovered 20 years ago,

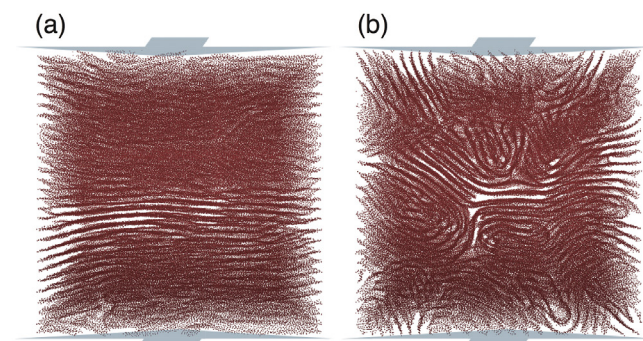


Fig. 1. Snapshot of surfactant membranes in simple shear flow. (a) A planar lamellae structure is formed at a low shear rate. (b) At a high shear rate, a rolled lamellar structure is formed perpendicularly to the flow direction. Top and bottom arrows represent the flow directions. The membranes are viewed from the flow direction.

the formation mechanism is not understood so far. Since the onion size is in a micro meter scale, it is far beyond applicable length scales for molecular simulations. Thus, we employed a highly coarse-grained membrane model, a meshless-membrane model, in which a membrane particle represents not a lipid molecule but a patch of the bilayer membrane. The particles self-assemble into membranes via multibody potential interactions.

At low shear rates, planar lamellae structures are formed at large membrane volume fractions (see Fig. 1a). At high shear rates, lamellar states exhibit undulation instability, leading to rolled or cylindrical membrane shapes oriented in the flow direction (see Fig. 1b). At even higher shear rate, the planar lamellae structures are formed again. The spatial symmetry and the structure factor of this rolled state agree with those of intermediate states during lamellar-to-onion transition measured by time-resolved small angle neutron and X-ray scattering experiments. A cylindrical or wavy lamellar structure was speculated to be this intermediate structure, but could not be distinguished from the scattering pattern alone. Our simulation results revealed that it is a rolled structure instead of regular cylindrical or wavy structures. The planar membranes become unstable in the flow gradient direction so that the membranes are rolled in perpendicular to the flow direction. We have not reproduced the onion structure itself. We will investigate the effects of defects and finite system size to pursue understanding of the onion phase.

Reference

[1] H. Shiba, H. Noguchi, and G. Gompper, *J. Chem. Phys.* **139**, 014702 (2013).

Authors

H. Shiba, H. Noguchi, and G. Gompper^a

^aForschungszentrum Juelich

Neutron Scattering Study on Alternating Spin-3/2 Chain Compound YCrGeO₅

M. Hase, T. Masuda, and K. Kindo

Neutron scattering technique is known as a powerful tool to probe the spin correlation in magnetic materials. Among various types of neutron instruments the chopper spectrometer is designed particularly for collecting inelastic neutron scattering (INS) spectrum. Combination of position sensitive detectors and accumulative data-acquiring system leads to a state-of-art instrument for measuring the dynamical structure factor $S(\mathbf{q}, \omega)$. Neutron Scattering Laboratory operates the High Resolution Chopper (HRC) spectrometer installed in J-PARC/MLF. The instrument covers the incident neutron energy range $10 \text{ meV} \leq E_i \leq 500 \text{ meV}$ and the scattering angle range $0.3^\circ \leq \psi \leq 40^\circ$, which meets typical magnetic scattering in most of magnetic materials. In this highlight we introduce a recent study on an alternating spin-3/2 chain compound by using the HRC spectrometer.

The phase diagrams of the alternating spin chain systems for various magnitudes of spin were extensively studied theoretically [1-4]. The model Hamiltonian is $\mathcal{H} = J \sum_i (1 - (-1)^i \delta) S_i \cdot S_{i+1}$. In case of spin-3/2 chain the spin alternation δ induces a spin gap at $0 < \delta < 0.42(2)$ and $0.42(2) < \delta \leq 1$, and the ground state is non-magnetic singlet. Tomonaga-Luttinger liquid (TTL) state exists at $\delta = 0$ and

$0.42(2)$. So far no experimental study has been reported because of absence of the model compound. Recently we found that RCrGeO₅ is a rare experimental realization of the spin-3/2 alternating spin chain. In this study we performed inelastic neutron scattering experiments on the polycrystalline sample of YCrGeO₅ to observe the magnetic excitation and to identify the spin Hamiltonian.

INS spectrums are shown in Figs. (a) and (b). The excitations are observed in the energy range of $8 \text{ meV} \leq \hbar\omega \leq 23 \text{ meV}$ at 4.0 K and the intensity decreases with the increase of Q . The intensity is suppressed at higher temperature of 199 K. The results mean that the observed excitations are dominated by magnetic scattering. No excitation is observed at $\hbar\omega \leq 8 \text{ meV}$ and this reveals the existence of the spin gap. The obtained powder INS spectrum was converted to the one-dimensional $S(q, \omega)$ [5] as shown in Fig. (c). The obtained profile was reproduced by empirical dispersion formula $\hbar\omega = \sqrt{A^2(\sin k)^2 + \Delta^2}$ with the parameters $\Delta = 10 \text{ meV}$ and $A = 20 \text{ meV}$. Figure (d) shows the dynamical structure factor calculated by DMRG with $\delta = 0.75$ and $\Delta/J=1.1$ and the calculation is consistent with the experiment. The measured magnitude of the spin gap is $\Delta = 10 \text{ meV}$

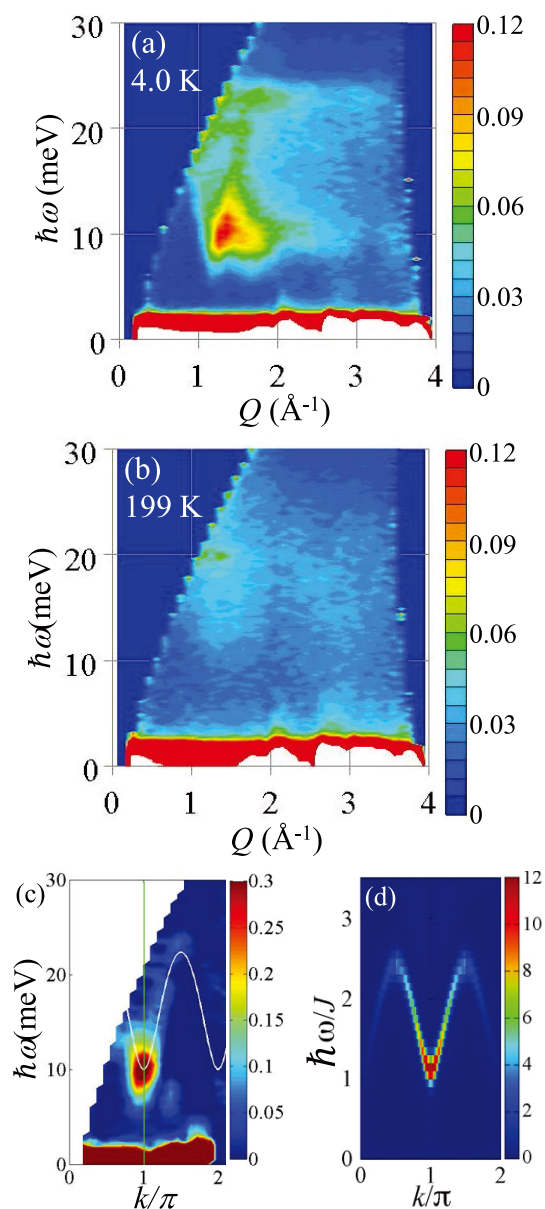


Fig. 1. (a) Inelastic neutron scattering (INS) spectrum of YCrGeO₅ at 4.0 K. (b) INS spectrum of YCrGeO₅ at 199 K. (c) INS spectrum converted to one-dimensional dynamical structure factor. (d) Calculated dynamical structure factor by DMRG method.

and this leads to $J = 11\text{meV}$. By using these parameters the magnetic susceptibility was quantitatively reproduced. Thus our study revealed that YCrGeO_5 is the first experimental realization of the spin-3/2 alternating spin chain.

As shown in Figs. (a) and (b) INS spectrum with high experimental resolution can be efficiently collected by using HRC spectrometer. Although the polycrystalline sample form, one-dimensional $S(q,\omega)$ can be obtained by the elaborated analysis. Combination of chopper spectrometer and polycrystalline sample will be a defacto standard in forthcoming era of neutron science.

References

- [1] Y. Kato and A. Tanaka, J. Phys. Soc. Jpn. **63**, 1277 (1994).
- [2] M. Kohno, M. Takahashi, and M. Hagiwara, Phys. Rev. B **57**, 1046 (1998).
- [3] M. Yajima and M. Takahashi, J. Phys. Soc. Jpn. **65**, 39 (1996).
- [4] S. Yamamoto, Phys. Rev. B **55**, 3603 (1997).
- [5] K. Tomiyasu, M. Fujita, A. I. Kolesnikov, R. I. Bewley, M. J. Bull, and S. M. Bennington, Appl. Phys. Lett. **94**, 092502 (2009).

Authors

M. Hase^a, M. Soda, T. Masuda, D. Kawana, T. Yokoo^b, S. Itoh^b, A. Matsuo, K. Kindo, and M. Kohno^a
^aNational Institute for Materials Science (NIMS)
^bHigh Energy Accelerator Research Organization (KEK)

Detection of Berry's Phase in a Bulk Rashba Semiconductor

H. Murakawa, M. Tokunaga, and Y. Tokura

The geometrical information of the system parameter can be encoded in the wave function as a Berry's phase and governs the system properties. In quantum systems, Berry's phase can be a source for various emergent phenomena. Despite its ubiquity, there are few experimental observations of Berry's phase of bulk states. Here, we report detection of a nontrivial π Berry's phase in the bulk Rashba semiconductor BiTeI via analysis of the Shubnikov-de Haas (SdH) effect.

BiTeI has a polar crystal structure made up of stacked layers of bismuth (Bi), tellurium (Te) and iodine (I) atoms. Because of the absence of inversion symmetry and the strong polarity of the system, accompanied by the strong spin-orbit interaction of Bi, an extremely large Rashba spin splitting occurs in a bulk scale (Fig. 1A). As shown in Fig. 1B, two coaxial spin polarized Fermi surfaces verging

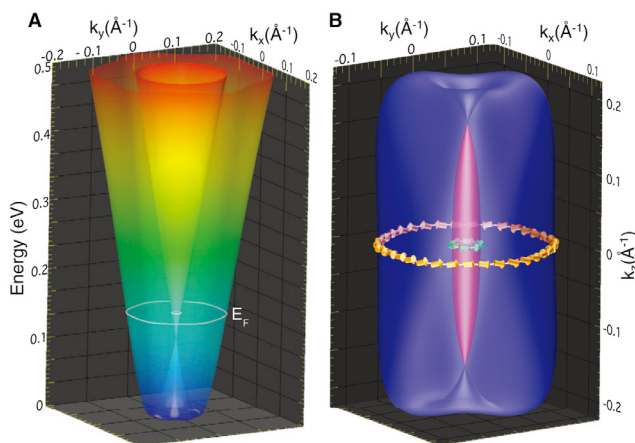


Fig. 1. (A) Energy band dispersion of the Rashba spin split band in BiTeI. (B) The inner and outer Fermi surfaces and helical spin textures (arrows) in BiTeI.

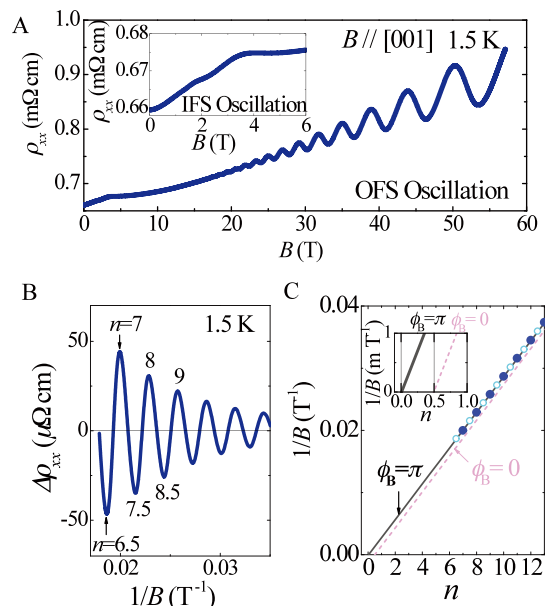


Fig. 2. (A) Magnetoresistivity of BiTeI sample. (B) The oscillatory component as a function of $1/B$. (C) Landau index plot of the outer Fermi. (inset) Magnified view around the intercept.

at Dirac point, namely, inner and outer Fermi surfaces (IFS and OFS, respectively) are formed. Theoretical prediction indicates that electrons on both FSs with the circular spin texture acquire π Berry's phase ($\phi_B = \pi$) and varies the system energy from the trivial case ($\phi_B = 0$). Under magnetic field, Landau levels in a Dirac system with $\phi_B = \pi$ locate at the middle of those in a system with $\phi_B = 0$. Thus, π Berry's phase can be detected as a π phase shift in quantum oscillation.

The extremely large Rashba spin splitting in BiTeI has great advantages on observing the Berry's phase. The large ratio of the extremal cross-sectional areas (A_N) of IFS and OFS enables the clear separation of the two sets of SdH oscillations. Moreover, the giant Rashba energy can dominate the Zeeman effect and preserve the circular spin texture even in a high magnetic field region. According to the Lifshitz-Onsager quantization rule, $A_N \hbar / eB = 2\pi(n + 1/2 - \phi_B/2\pi) = 2\pi(n + \gamma)$, Berry's phase is obtained as an intercept value γ in the linear relation between $1/B$ and Landau index number n . For precise evaluation, observation of the SdH oscillation down to lower Landau level is important. Therefore, high-magnetic field measurement with use of the non-destructive pulse magnet can be a powerful tool. Figure 2A shows the SdH oscillation from the OFS up to 56 T. We assign integer indices to the ρ_{xx} peak positions in $1/B$ and half integer indices to the ρ_{xx} valley positions (Fig. 2B). As shown in Fig. 2C, the interpolation line has almost zero intercept ($\gamma = 1/2 - \phi_B/2\pi = 0$), confirming the existence of π Berry's phase in the 3-dimensional Rashba semiconductor BiTeI.

Reference

- [1] H. Murakawa, M. S. Bahramy, M. Tokunaga, Y. Kohama, C. Bell, Y. Kaneko, N. Nagaosa, H. Y. Hwang, and Y. Tokura, Science **342**, 1490 (2013).

Authors

H. Murakawa^a, M. S. Bahramy^b, M. Tokunaga, Y. Kohama, C. Bell^c, Y. Kaneko^a, N. Nagaosa^{a,b}, H. Y. Hwang^{a,c}, and Y. Tokura^{a,b}
^aRiken CEMS
^bThe University of Tokyo
^cStanford University

Discovery of Novel Phase of Solid Oxygen in Ultrahigh Magnetic Fields

T. C. Kobayashi and Y. H. Matsuda

Molecular oxygen has the spin $S = 1$ and the relation between the magnetic interaction and the crystal structure has been attracting attention of material scientists for a long time [1]. In the present work, we discovered a novel phase of solid oxygen as a result of the first-order structural phase transition by applying an extraordinarily strong magnetic field of up to 193 Tesla [2]. The change in the crystal symmetry due to the rearrangement of O_2 molecules is strongly suggested, which can make the new oxygen phase ferromagnetic. Since all known seven phases of solid oxygen have the antiferromagnetic nature, it is remarkable to obtain ferromagnetic oxygen.

The magnetization and magneto-transmission measurements have been performed in ultrahigh fields using a destructive manner, the single-turn coil technique. The magnetic field was applied in the α -phase of solid oxygen at low temperatures ($T < 24$ K). As shown in Fig. 1, we found that the magnetization rapidly increased at around 125 T. This is a clear evidence of the field-induced magnetic phase transition. Since the magnetization process has the large hysteresis, the transition is expected to be of first order. Figure 2 shows the time dependence of the magnetic field and two-dimensional magneto-transmission image. You can see that something drastic happens at very high magnetic fields. The field where this phenomenon is seen almost corresponds to the critical field of the magnetization jump shown

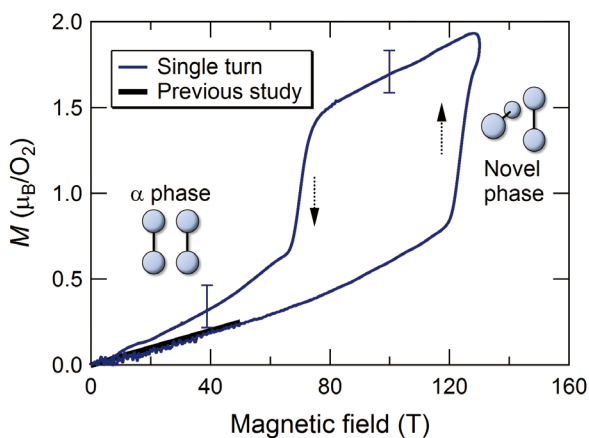


Fig. 1. The magnetization curve in α -oxygen at 9 K up to 129 T.

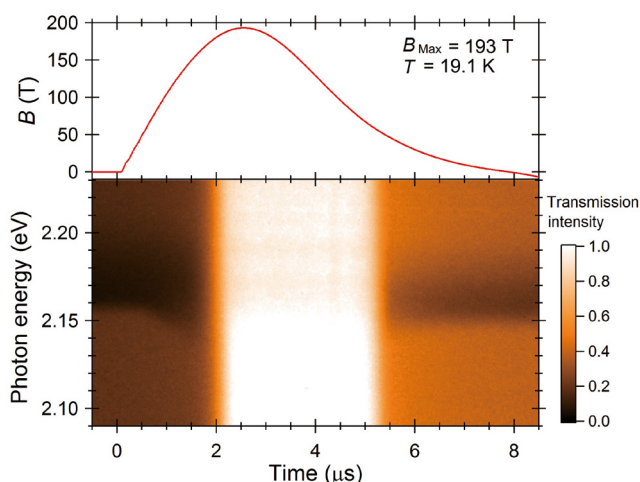


Fig. 2. (a) The waveform of the pulsed magnetic field. (b) The two-dimensional magneto-transmission image of α -oxygen.

in Fig. 1.

The structural phase transition along with the magnetic transition explains the experimental findings; the significant increase of the light transmission is due to the reduction of the classical light scattering at the domain boundaries. In the strong magnetic field, the crystal structure becomes isotropic (cubic) from the anisotropic one (monoclinic). The origin of the phase transition is suggested to be the rearrangement of O_2 molecules, which is driven by the change in the exchange interaction depending on the spatial arrangement of the O_2 molecules.

The discovered novel phase is the eighth phase of solid oxygen, which has the different geometry of O_2 molecules from other seven phases. The state-of-the-art high magnetic field technique was essential in this discovery. Nowadays, in materials science, many treasures waiting for discovery are expected at the frontier of extreme high field.

References

- [1] Y. A. Freiman, and H. J. Jodl, Phys. Rep. **401**, 1 (2004) and references therein.
- [2] T. Nomura, Y. H. Matsuda, S. Takeyama, A. Matsuo, K. Kindo, J. L. Her, and T. C. Kobayashi, Phys. Rev. Lett., Editors' Suggestion, (2014) in press.

Authors

T. C. Kobayashi^a, T. Nomura, Y. H. Matsuda, S. Takeyama, A. Matsuo, K. Kindo, and J. L. Her^b
^aOkayama University
^bChang Gung University

Structure Determination of Silicene on Ag(111) by Low-Energy Electron Diffraction

K. Kawahara, T. Shirasawa, and N. Takagi

Silicene, a 2-dimensional honeycomb lattice of Si, attracts much attention since it is predicted to acquire exotic features such as massless Dirac fermions and high electron mobility [1]. As the spin orbit coupling of Si is 1000 times larger than that of C, silicene is one of the most interesting candidates for 2-dimensional topological insulator [2]. In addition, silicene should match with the current Si based technology. These characteristics make silicene promising in the next generation devices.

Several groups reported synthesis of silicene on Ag(111) [3-8]. Silicene forms 4×4 superstructure on the Ag(111) surface [4-8]. On a fundamental question 'Does 4×4 silicene have Dirac fermions?', the arguments conflict among the research groups [4,7]. The electronic structure is connected with the atomic arrangement. Thus, by determining the atomic position, we can answer the above question. However, the geometric structure of 4×4 silicene has not been established. Several groups proposed the structural models of 4×4 silicene based on the result of scanning tunneling microscopy (STM) [4-8]. The reasonable model is a buckled structural model constructed by the STM and density functional theory (DFT) calculations [4-7]. In contrast, Feng *et al.* claimed that the corner-hole like features observed in the STM image are assigned to missing Si atoms and proposed a model in which hydrogen atoms terminate the dangling bonds of Si atoms [8]. The discrepancy arises from that the STM image is convolution of the geometric structure together with the electronic density of states. Hence we cannot determine the positions of the individual atoms in the 4×4 silicene only by

Observing Hot Carrier Distribution in an n-type Epitaxial Graphene on a SiC Substrate

H. Fukidome and I. Matsuda

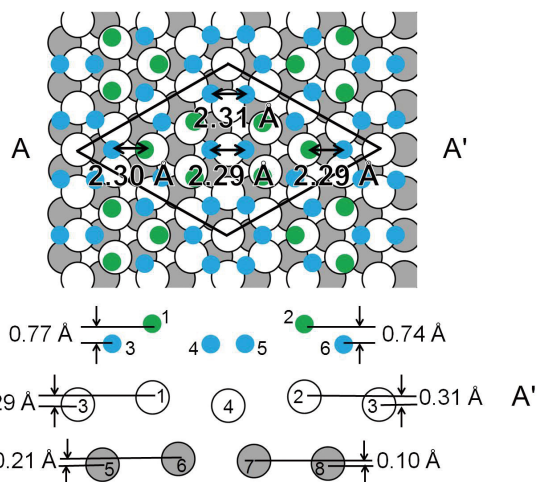


Fig. 1. The top and side views of the best-fit structure of 4×4 silicene. The side view is the cross section along the AA'. Green and blue balls represent Si atoms. The green Si atoms are moved up to the vacuum. White and Gray balls represent Ag atoms in the first and second layer, respectively.

STM measurements.

Electron diffraction is one of the most reliable and powerful techniques to determine the geometric structure. We have determined the geometric structure of 4×4 silicene by using low-energy electron diffraction [9]. We examined the regularly-buckled silicene, the buckled structure where six Si atoms are displaced and the structural model proposed by Feng *et al.* The optimized reliability factor (R-factor) of the buckled structure shown in Fig. 1 was 0.17. The optimized R factor of the model proposed by Feng *et al.* [8] was 0.48. The buckled structural model as Fig. 1 reproduced the experimental results very well. Figure 1 shows the top and cross sectional views of the best-fit structural model for 4×4 silicene. The green Si atoms are displaced perpendicularly to the surface and silicene forms into a buckled structure. The Si-Si bond lengths range from 2.29 to 2.31 Å, which are shorter than that for the bulk diamond structure. Substrate Ag atoms are displaced vertically at the interface. The R-factor is 0.52 for the model without the displacement of Ag, indicating that the displacement of Ag atoms is a key factor to determine the structure of 4×4 silicene. The displacement of Ag also reflects the strong interaction between silicene and Ag substrate, supporting the experimental results showing absence of the Dirac fermions [7]. In addition, the experimentally determined structure of 4×4 silicene matches quite well with that optimized by DFT calculations [4,5]. Thus, the geometric structure of 4×4 silicene on Ag(111) was completely clarified.

References

- [1] S. Cahangirov *et al.*, Phys. Rev. Lett. **102**, 236804 (2009).
- [2] M. Ezawa, Phys. Rev. Lett. **109**, 055502 (2012).
- [3] B. Lalmi *et al.*, Appl. Phys. Lett. **97**, 223109 (2010).
- [4] P. Vogt *et al.*, Phys. Rev. Lett. **108**, 155501 (2012).
- [5] C.-L. Lin *et al.*, Appl. Phys. Express **5**, 045802 (2012).
- [6] R. Arafune *et al.*, Surf. Sci. **608**, 297 (2013).
- [7] C.-L. Lin *et al.*, Phys. Rev. Lett. **110**, 076801 (2013).
- [8] B. Feng *et al.*, Nano Lett. **12**, 3507 (2012).
- [9] K. Kawahara *et al.*, Surf. Sci. **623**, 25 (2014).

Authors

K. Kawahara^a, T. Shirasawa, R. Arafune^b, C.-L. Lin^a, T. Takahashi, M. Kawai^a, and N. Takagi^a
^aThe University of Tokyo
^bIMANA-NIMS

A monolayer graphene is "supermaterial" that is the thinnest, lightest, and strongest material with ultrahigh electrical and thermal conductivity. Recently optical properties of the graphene have also attracted interests in the field of developing optoelectronic, plasmonic and nanophotonic devices. However, detailed mechanisms of the photo-induced phenomena of a graphene, such as the multiple carrier generation, have not been understood and, thus, the direct investigation of the non-equilibrium carrier dynamics has been strongly called for.

In the present research, we carried out femtoseconds(fs)-time- and angle-resolved photoemission experiment to observe the temporal variation of the Dirac electrons after the optical pumping in *real time*. The measurement was carried out using high-harmonic generation (HHG) laser system based on the Ti:Sapphire laser ($h\nu=1.57$ eV). Photon energy of 28.26 eV for the HHG laser pulse is generated by irradiating the second harmonic laser pulses ($h\nu =3.14$ eV) at Ar gas and it is high enough to cover the electron momentum of the Dirac band at the K point in angle-resolved photoemission measurement. The time-resolved data were obtained using the pump (3.14 eV laser) and probe (HHG) method with a repetition rate of 1 kHz.

Figure 1(a) shows a series of angle-integrated spectra taken with a laser pumping power of 2.5 mW at various delay times. Dispersion of the Dirac bands, observed by angle-resolved photoemission at the K point, is shown in the inset. With laser pumping ($t=0$), the photoemission intensity of the upper Dirac band (UDB) decreases significantly while that of the lower Dirac band (LDB) remains constant. Around the energy corresponding to the Fermi energy, the spectral tail extends in energy. The slope of the spectral edge also becomes small. At each delay time, the

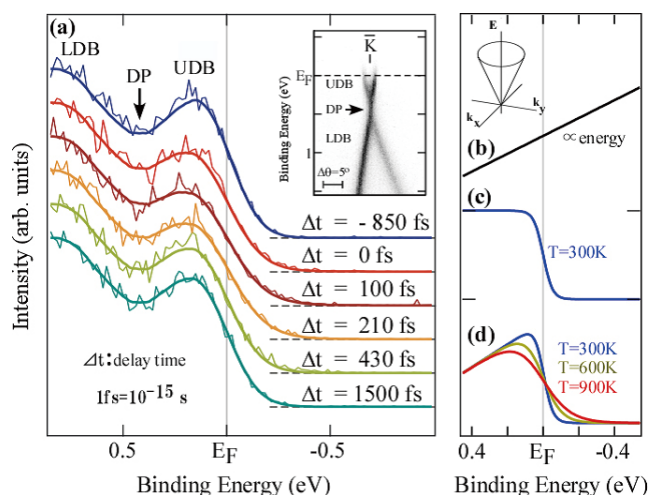


Fig. 1. (a) Comparison of the spectra at different delay times. The experimental spectra were taken at a photon energy of 28.26 eV at various delay times with pumping laser irradiation ($h\nu=3.14$ eV). The intensity variation for the UDB is clearly reproduced by the simulated result (d) while the intensity for the LDB is unchanged. The inset shows dispersion of the Dirac bands near the Fermi level (E_F). The upper Dirac band (UDB) and lower Dirac band (LDB) are labeled in the figure and the Dirac Point (DP) is indicated by an arrow. (b)–(d) Simulation of energy spectra for two cases of Dirac free electrons. The inset shows their two-dimensional band dispersion. (b) density of states, (c) Fermi–Dirac function, and (d) resulting spectra.

raw experimental data, drawn with thin colored lines, are curve-fitted with a function that is a product of density of states of graphene, Fig. 1 (b), and the Fermi-Dirac function, Fig. 1(c). In the spectral simulation of Fig. 1 (d), the Fermi edge shows a peak-like structure, and the peak top shifts toward higher binding energy at higher temperature. In Fig. 1(a), the fitting results are drawn through raw experimental data with bold colored lines. The temporal evolution in Fig. 1(a) is described by comparing it with the intensities simulated in Fig. 1(d), and it reflects the time evolution of the electronic temperature, that is, the transient distribution of the hot carriers (electrons).

Reference

[1] T. Someya, H. Fukidome, Y. Ishida, R. Yoshida, T. Iimori, R. Yukawa, K. Akikubo, Sh. Yamamoto, S. Yamamoto, T. Yamamoto, T. Kanai, K. Funakubo, M. Suemitsu, J. Itatani, F. Komori, S. Shin, and I. Matsuda, *Appl. Phys. Lett.* **104**, 161103 (2014).

Authors

I. Matsuda, H. Fukidome^a, J. Itatani, S. Shin, and F. Komori
^aTohoku University

Electronic Structure of Carbon-Related Catalysts During Fuel Cell Operation by Soft X-Ray Emission Spectroscopy

H. Niwa, Y. Harada, and M. Oshima

Polymer electrolyte fuel cells (PEFCs) are expected to be promising power sources of high efficiency, low operating temperature, and low pollution for transportation and residential applications. Recently, carbon-based catalysts are getting considerable attention since adequately designed carbon-based catalysts show high ORR activities and are expected to be cathode catalysts alternative to conventional Pt-based catalysts [1,2]. The origin of their high ORR activities should be elucidated to further enhance the activities for commercialization. Previous electronic structure studies on carbon-based catalysts were mostly done at ex situ condition[3]. However, the results were not always conclusive because they did not observe the chemical state of each element under PEFC working condition. To further explore the ORR mechanism of carbon-based cathode catalysts,

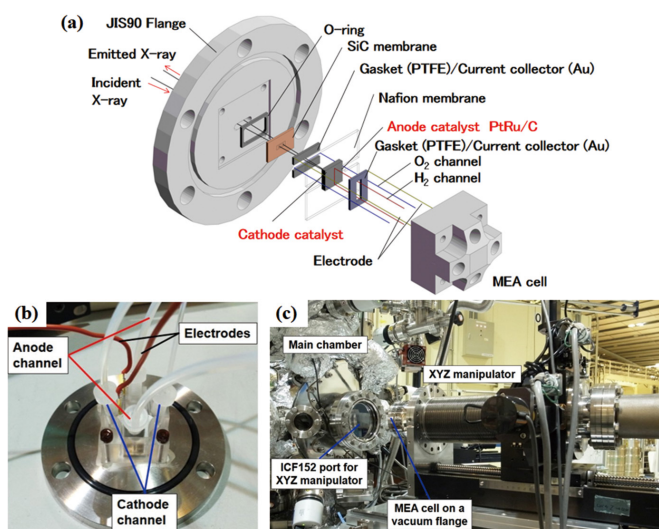


Fig. 1. (a) Schematic view of the MEA cell for operando SXE measurements. (b) Photograph of the MEA cell on a vacuum flange. (c) Photograph of a XYZ manipulator and a main chamber.

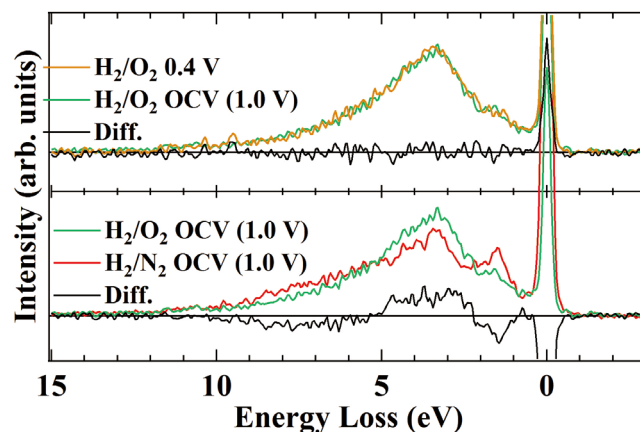


Fig. 2. Smoothed Fe 2p SXE spectra compared with the open circuit voltage (lower panel) and the same gas condition (upper panel). Black solid lines are difference spectra.

operando observation of the electronic structure is strongly required.

Here we report a novel electrochemical cell system developed for operando soft X-ray emission spectroscopy of cathode catalysts for polymer electrolyte fuel cells at BL07LSU of SPring-8[4]. Incorporating a membrane electrode assembly on a vacuum compatible flange (Fig. 1), the system enables direct observation of element-specific electronic structure that changes with gaseous and potential conditions for electrochemical reaction. We have successfully observed the electronic structure of iron in the iron phthalocyanine-based cathode catalyst under various working conditions by the operando soft X-ray emission spectroscopy. At open circuit voltage it is found that an oxidized iron site exists even after reductive high temperature pyrolysis and is active for oxygen adsorption (Fig. 2), which is not expected from ex situ results for powder samples where metallic iron site inactive for ORR dominates.

References

- [1] W. Y. Wong, W. R.W. Daud, A. B. Mohamad, A. A. H. Kadhum, E. H. Majlan, and K. S. Loh, *Diam. Relat. Mater.* **22**, 12 (2012).
- [2] F. Jaouen, E. Proietti, M. Lefèvre, R. Chenitz, J.-P. Dodelet, G. Wu, H. T. Chung, C. M. Johnston, and P. Zelenay, *Ene. Environ. Sci.* **4**, 114 (2011).
- [3] U. I. Kramm, I. Abs-Wurmbach, I. Herrmann-Geppert, J. Radnik, S. Fiechter, and P. Bogdanoff, *J. Electrochem. Soc.* **158**, B69 (2011).
- [4] H. Niwa, H. Kiuchi, J. Miyawaki, Y. Harada, M. Oshima, Y. Nabae, and T. Aoki, *Electrochem. Commun.* **35**, 57 (2013).

Authors

H. Niwa, H. Kiuchi^a, J. Miyawaki, Y. Harada, M. Oshima^a, Y. Nabae^b, and T. Aoki^c
^aThe University of Tokyo
^bTokyo Institute of Technology
^cToshiba Fuel Cell Power Systems Corporation

Clarification of Mechanism of Ferromagnetism in Ferromagnetic Semiconductor

M. Kobayashi, A. Tanaka, and Y. Harada

A ferromagnetic semiconductor (FMS), in which a host semiconductor is doped with a low concentration of magnetic ions, has attracted much attention in spintronics, which exploits the properties of magnets for electronics

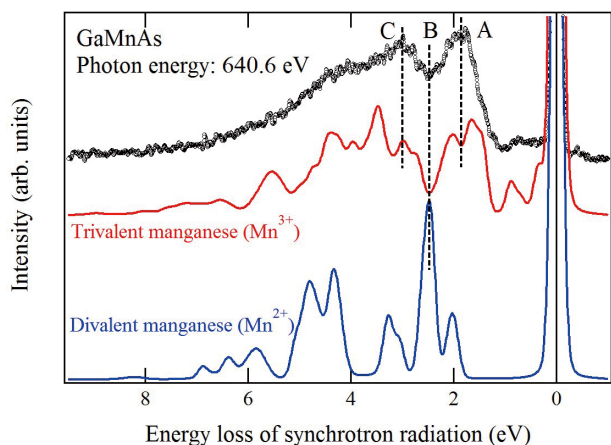


Fig. 1. Soft X-ray emission spectrum of GaMnAs and simulation results. The simulation result for Mn^{3+} (red) is in good agreement with the experimental spectrum (black).

indispensable in industry. These semiconductors have both electrical properties of a semiconductor and magnetic properties of a doped magnetic element. $Ga_{1-x}Mn_xAs$ (GaMnAs) is a typical ferromagnetic semiconductor obtained by doping a small amount of manganese (Mn) into gallium arsenide (GaAs). Its practical application as a spintronics material is being examined because it exhibits ferromagnetism at a relatively high temperature. However, the mechanism of ferromagnetism in GaMnAs has not been conclusively determined, and various physical models have been proposed.

In this study, to address the electronic structure of the doped Mn ions, we report the results of Mn L_3 x-ray absorption spectroscopy (XAS) and resonant inelastic x-ray scattering (RIXS) measurements of $Ga_{1-x}Mn_xAs$ ($x = 0.04$) at SPring-8 BL23SU and BL07LSU [1], respectively. RIXS is a powerful tool to investigate electronic excitations in element- and symmetry-specific ways including $d-d$ and charge-transfer (CT) excitations for open shell $3d$ orbitals [2], and magnetic excitations for spin or charge-ordered systems [3]. These excitations are sensitive to electron correlation, crystalline symmetry, and the strength of hybridization with the ligand band. The RIXS spectra obtained for $Ga_{1-x}Mn_xAs$ are compared with configuration-interaction (CI) cluster-model calculations [4], and the electronic structure parameters are estimated.

The obtained XAS spectrum was compared with the CI cluster model calculations. Both the calculated spectra for the Mn^{2+} and Mn^{3+} states well reproduce the experimental XAS spectrum and we cannot determine the effective charge on the Mn site. On the other hand, the RIXS spectra provide definitive information: the RIXS spectra in Fig. 1 show a broad profile even at energy resolutions high enough to distinguish individual $d-d$ excitation peaks of MnO. An analysis by the CI calculations indicates that the Mn ground

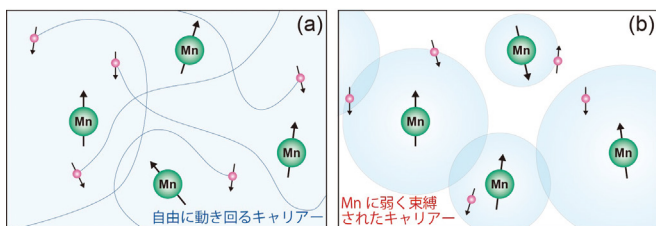


Fig. 2. Models for mechanism of ferromagnetism in $Ga_{1-x}Mn_xAs$: (a) Zener's $p-d$ exchange model and (b) magnetic polaron model. The direction of the arrows in the upper figure indicates the direction of magnets.

states mainly consist of the Mn^{3+} electronic configuration composed of the charge-transferred states ($d^5\bar{L}$ and $d^5\bar{L}^2$), in which the ligand hole is weakly bound to the Mn $3d$ state (which can be explained by the magnetic polaron model: Fig. 2(b)), rather than the pure Mn^{2+} state (which can be explained by the Zener's $p-d$ exchange model: Fig. 2(a)). In order to reproduce the experimental broadening of the Mn $d-d$ excitation, not only the (Gaussian) broadening by the energy resolution but also the 0.5 eV Lorentzian broadening is required. The additional Lorentzian broadening in the RIXS spectra can be attributed to the lifetime broadening in the final state of the RIXS process where fast decay of the $d-d$ excitations to an electron-hole pair in the host valence and conduction bands occurs because of the hybridization between the Mn $3d$ orbital and the ligand band.

References

- [1] G. Ghiringhelli, M. Matsubara, C. Dallera, F. Fracassi, A. Tagliaferri, N. B. Brookes, A. Kotani, and L. Braicovich, *Phys. Rev. B* **73**, 035111 (2006).
- [2] M. L. Tacon, G. Ghiringhelli, J. Chaloupka, M. M. Sala, V. Hinkov, M. W. Haverkort, M. Minola, M. Bakr, K. J. Zhou, S. Blanco-Canosa, C. Monney, Y. T. Song, G. L. Sun, C. T. Lin, G. M. D. Luca, M. Salluzzo, G. Khalullin, T. Schmitt, L. Braicovich, and B. Keimer, *Nat. Phys.* **7**, 725 (2011).
- [3] A. Tanaka and T. Jo, *J. Phys. Soc. Jpn.* **63**, 2788 (1994).

Authors

M. Kobayashi^a, H. Niwa^a, Y. Takeda^b, A. Fujimori^a, Y. Senba^c, H. Ohashi^c, A. Tanaka^a, S. Ohya^a, P. N. Hai^a, M. Tanaka^a, Y. Harada, and M. Oshima^a

^aThe University of Tokyo

^bJapan Atomic Energy Agency

^cJapan Synchrotron Radiation Research Institute (JASRI)

^dHiroshima University

Selective Probing of the OH or OD Stretch Vibrations in Liquid Water Using Resonant Inelastic Soft X-ray Scattering

Y. Harada, T. Tokushima, and S. Shin

The unique property of water, such as high boiling and melting point compared to molecules like non-metal hydride, or less density in solid form than in liquid form, are

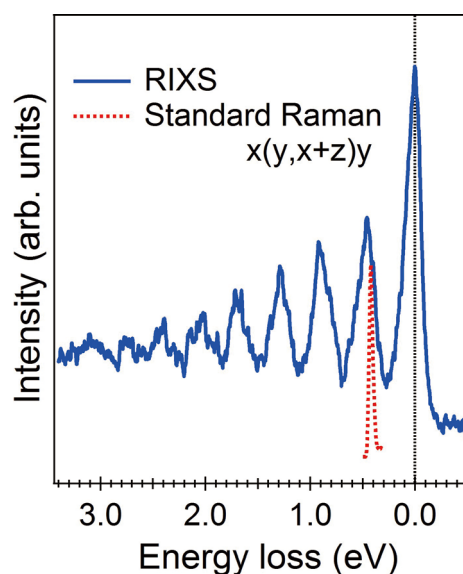


Fig. 1. The water vibronic structure observed in the RIXS spectrum. Dotted red curve is a standard Raman spectrum of liquid water in the same experimental configuration $x(y, x+z)y$ [2] as the O 1s RIXS.

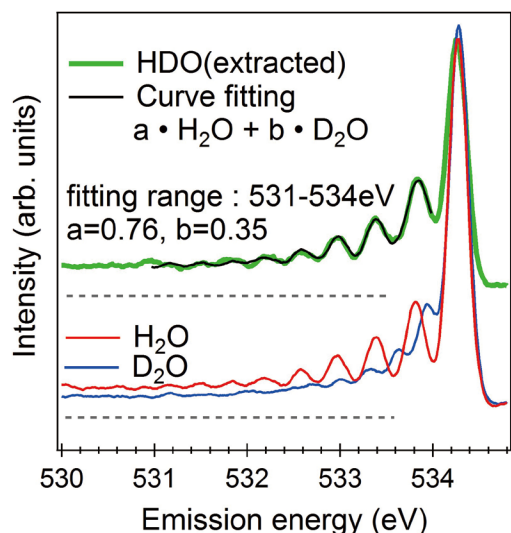


Fig. 2. Isotope effect on the multiple vibrational excitations of water. For each spectrum the background level is indicated by a dashed line. The extracted HDO spectrum is fitted with a linear combination of the H₂O and D₂O spectra in the range from 531–534 eV.

explained by an attractive force between water molecules, called 'hydrogen bond'. There are many proposed local structural models that describe the water network. Among them, a continuum model, where hydrogen bonds in water are distorted, broken and reformed continuously, but water itself is composed of a single component, or a mixture (micro-heterogeneity) model, where the network is considered as a mixture of various hydrogen bond configurations, are well known. However, the model that describes better the hydrogen bond property of liquid water, is still under debate.

In this work, we have succeeded in revealing validity of the mixture (micro-heterogeneity) model by selective observation of hydrogen-bond-broken water molecules and in detecting with high sensitivity the difference in the degree of hydrogen bond strength between light (normal) water and heavy water (in which both hydrogen atoms have been replaced with deuterium) using soft X-ray resonant inelastic scattering at BL07LSU and BL17SU of SPring-8[1]. High-resolution O 1s resonant inelastic X-ray scattering spectra of liquid H₂O/D₂O/HDO, obtained by excitation near the pre-edge resonance (Fig. 1) show, in the elastic line region, well-separated multiple vibrational structures corresponding to the internal OH stretch vibration in the ground state of water. The energy of the first-order vibrational excitation is strongly blue-shifted with respect to the main band in the Infrared/Raman spectra of water [2], indicating that water molecules with a highly weakened or broken donating hydrogen bond are correlated with the pre-edge structure in the X-ray absorption spectrum. As shown in Fig. 2, the vibrational profile of pre-edge excited HDO water is well fitted with 50±20% greater OH-stretch contribution compared to OD, which strongly supports a preference for OH being the weakened or broken H-bond in agreement with the well-known picture that D₂O makes stronger H-bonds than H₂O [3,4]. Accompanying path-integral molecular dynamics simulations show that this is particularly the case for strongly asymmetrically H-bonded molecules, i.e. those that are selected by pre-edge excitation. These results are expected to lead to the clarification of the role of water in various chemical and catalytic reactions as well as water in biological organisms where hydrogen bond plays an important role.

References

[1] Y. Harada, T. Tokushima, Y. Horikawa, O. Takahashi, H. Niwa,

M. Kobayashi, M. Oshima, Y. Senba, H. Ohashi, K. T. Wikfeldt, A. Nilsson, L. G. M. Pettersson, S. Shin, *Phys. Rev. Lett.* **111**, 193001 (2013).
 [2] G. E. Walrafen, M. S. Hokmabadi, and W.-H. Yang, *J. Chem. Phys.* **85**, 6964 (1986).
 [3] J.D. Smith, C. D. Cappa, K. R. Wilson, R. C. Cohen, P. L. Geissler, R. J. Saykally, *Proc. National Acad. Sci. (USA)* **102**, 14171 (2005).
 [4] Y. Nagata, R.E. Pool, E.H.G. Backus, M. Bonn, *Phys. Rev. Lett.* **109**, 226101 (2012).

Authors

Y. Harada, T. Tokushima^a, Y. Horikawa, O. Takahashi^b, H. Niwa^c, M. Kobayashi^c, M. Oshima^c, Y. Senba^d, H. Ohashi^d, K. T. Wikfeldt^{e,f}, A. Nilsson^{g,h}, L. G. M. Pettersson^h, and S. Shin

^aRIKEN/SPring-8
^bHiroshima University
^cThe University of Tokyo
^dJASRI/SPring-8
^eUniversity of Iceland
^fNORDITA, AlbaNova University Center
^gSLAC National Accelerator Laboratory
^hAlbaNova University Center, Stockholm University

